26/14-95

ISSN 0234-5366



# КРАТКИЕ СООБЩЕНИЯ ОИЯИ

# JINR RAPID COMMUNICATIONS

3[71]-95

Monte Carlo Simulation of Silicon Detectors for the ALICE Experiment at LHC	u
A Study of Single Tagged Multihadronic $\gamma \gamma^*$ Events at an Average $Q^2$ of 90 GeV <sup>2</sup>	0
Epithermal Neutron Activation Analysis of Moss, Lichen and Pine Needles in Atmospheric Deposition Monitoring	0
To the Theory of Neutrino Oscillation	
Coupled Quadrupole and Monopole Vibrations of Large Amplitude	0
Test of the Ellis-Jaffe Sum Rule Using Parametrization of the Measured Lepton-Proton Asymmetry	0

Издательский отдел ОИЯИ

ДУБНА

Объединенный институт ядерных исследований Joint Institute for Nuclear Research

3[71]-95

JINR RAPID COMMUNICATIONS

# ОГЛАВЛЕНИЕ CONTENTS

B.Batyunya, A.Zinchenko
Monte Carlo Simulation of Silicon Detectors
for the ALICE Experiment at LHC
Б.Батюня, А.Зинченко
Монте-Карло моделирование кремниевых детекторов
для эксперимента АЛИСА на LHC
P. Detuurus I Diagna E Vanuata V Dagdayakay
B.Batyunya, J.Bjarne, F.Kapusta, V.Pozdnyakov,
I.Tyapkin, N.Zimin
A Study of Single Tagged Multihadronic γγ* Events
at an Average $Q^2$ of 90 GeV <sup>2</sup>
Б.Батюня, И.Бьярн, Ф.Капуста, В.Поздняков,
И.Тяпкин, Н.Зимин
Изучение меченых мультиадронных үү*-событий
при $\langle Q^2 \rangle \equiv 90 \ \Gamma \ni B^2$
V.M.Nazarov, M.V.Frontasyeva, V.F.Peresedov,
V.P.Chinaeva, T.M.Ostrovnaya, S.F.Gundorina,
V.V.Nikonov, N.V.Loukina
Epithermal Neutron Activation Analysis of Moss, Lichen
and Pine Needles in Atmospheric Deposition Monitoring
В.М.Назаров, М.В.Фронтасьева, В.Ф.Переседов,
В.П.Чинаева, Т.М.Островная, С.Ф.Гундорина,
В.В.Никонов, Н.В.Лукина
Эпитепловой нейтронный активационный анализ мхов,
лишайников и хвон сосны
в мониторниге атмосферных выпадений
Kh.M.Beshtoev
To the Theory of Neutrino Oscillation
Х.М.Бештоев
К теорин осцилляции нейтрино
E.B.Balbutsev, I.V.Molodtsova, P.Schuck
Coupled Quadrupole
and Monopole Vibrations of Large Amplitude
Е.Б.Бальбуцев, И.В.Молодцова, П.Шук
Связанные квадрупольные
и монопольные колебания большой амплитулы 30

A.P.Nagaitsev, V.G.Krivokhijine, I.A.Savin, G.I.Smirnov	
Test of the Ellis-Jaffe Sum Rule	
Using Parametrization of the Measured Lepton-Proton Asymmetry	
А.П.Нагайцев, В.Г.Кривохижин, И.А.Савин, Г.И.Смирнов	
Проверка правила сумм Эллиса — Джаффе	
с использованием параметризации	
принцу по пертон-протонной асиметрии	50

I was a series

УДК 539.1.074.55

# MONTE CARLO SIMULATION OF SILICON DETECTORS FOR THE ALICE EXPERIMENT AT LHC

#### B.Batyunya, A.Zinchenko

Some results of studies of silicon detector characteristics of the ALICE experiment are presented based on a «realistic» Monte Carlo simulation of the detector performance. The results obtained confirm general conclusions of the Letter of Intent. They also indicate some problems which have to be addressed in order to reach designed parameters.

The investigation has been performed at the Laboratory of High Energies, JINR.

## Монте-Карло моделированне кремниевых детекторов для эксперимента АЛИСА на LHC

#### Б.Батюня, А.Зинченко

Представлены результаты исследований характеристик кремниевых детекторов эксперимента АЛИСА, основанные на «реалистическом» Монте-Карло моделировании их работы. Полученные результаты подтверждают основные выводы проекта эксперимента. Они также указывают на некоторые проблемы, которые должны быть изучены, чтобы достичь запланированных параметров.

Работа выполнена в Лаборатории высоких энергий ОИЯИ.

#### 1. Introduction

In Ref. [1] we described a GEANT-based programme for a «realistic» simulation of silicon detectors of the ALICE experiment and presented some results demonstrating the programme performance. In this paper we show new results obtained during our continuing work on the ALICE silicon detector simulation.

## 2. Silicon Tracker Geometry

Description of the ALICE detector and simulation programme can be found in Refs. [1] and [2]. The silicon tracker includes five layers of silicon with the innermost layer being a pixel detector, next 3 layers being silicon drift detectors and the outermost one being a double-sided microstrip detector. The pixel detector has a pixel size of 75  $\mu$ m in r- $\phi$  and 270  $\mu$ m in z-direction, the silicon drift detector has the anode pitch of 250  $\mu$ m (in r- $\phi$ ) and

the drift direction along the beam line with the maximum drift distance of 35 mm, the double-sided microstrip detector has the strip pitch of 100  $\mu$ m and a stereo angle of 30 mrad. Charge collected on anodes of the silicon drift detector is digitized every 25 ns that corresponds to 150  $\mu$ m in space for the 6  $\mu$ m/nc drift velocity.

The following results were obtained using a simple algorithm of cluster finding in silicon detectors, i.e., a cluster was defined as any continuous group of charges exceeding some threshold value. We took the threshold to be equal to 0 for the case without noise added and  $4 \times \sigma_{\text{noise}}$  otherwise, where  $\sigma_{\text{noise}}$  is a standard deviation of the gaussian noise distribution equal to 500 electrons for the pixel and SDDs and  $1240e^-$  for the microstrip.

#### 3. Coordinate Resolution of Silicon Drift Detectors

It has been shown in [1] that effect of the electronic noise on coordinate resolution of silicon drift detectors is substantial at least when a coordinate is reconstructed as a simple center of gravity of a charge distributions in a cluster. It means that a good knowledge of noise conditions is essential for correct simulation. As expected in Ref. [3], the noise contribution to sequential time bins in SDDs will be highly correlated. It should result in resolution improvement in z-direction and deterioration in r- $\phi$ -direction in our case. We checked that by generating the correlated noise according to the two-dimensional gaussian distribution:

$$p(q_i, q_{i+1}) = \frac{1}{2\pi\sigma^2 \sqrt{1 - \rho^2}} \times \exp\left[-\frac{q_i^2 + q_{i+1}^2 - 2\rho q_i q_{i+1}}{2\sigma^2 (1 - \rho^2)}\right],$$
$$p(q_1) = \frac{1}{\sqrt{2\pi}\sigma} \times \exp\left[-\frac{q_1^2}{2\sigma^2}\right],$$

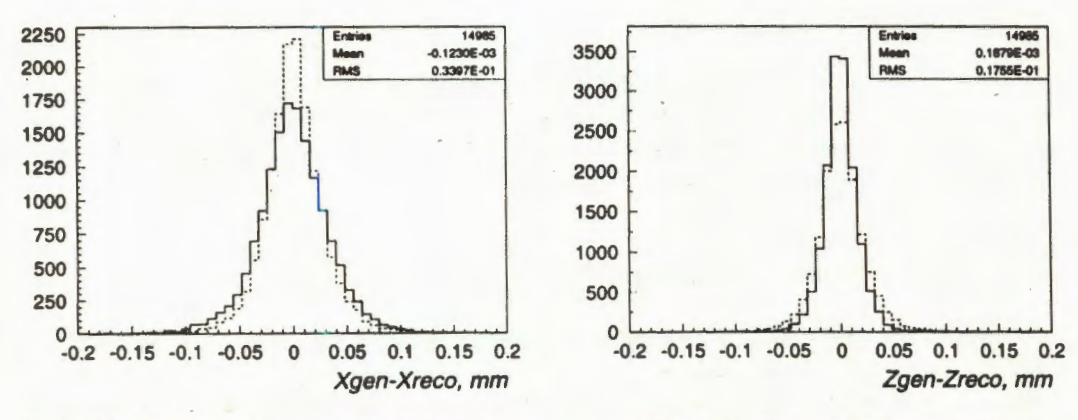
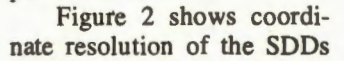


Fig.1. Distributions of  $x_{gen} - x_{reco}$  (left) and  $z_{gen} - z_{reco}$  (right) for silicon drift detectors with a correlated (full line) and uncorrelated (dashed line) noise

where  $q_1$ ,  $q_i$  are noise charges in the first and i-th bins, respectively: o is a standard deviation of the noise distribution and p is a correlation coefficient (we took it equal to 0.95 in our studies). The results obtained are shown in Fig.1, where differences of generated and reconstructed coordinates in azimuthal shown.  $(x_{\text{gen}} - x_{\text{reco}})$ These distributions were produced for muons with momenta of 6 + 10 GeV/c randomly distributed in angular intervals of - 180° + 180° in  $\phi$  and  $85^{\circ} + 95^{\circ}$  in  $\theta$ . As can be seen, the noise correlation changes the resolution in expected direction.



as a function of the drift distance for the case with a correlated noise. The shape of the dependence can be easily understood if one considers the number of anode pads or FADC bins which collect the charge released by a track. The resolution for long drift distances can be possibly improved using more sophisticated methods of coordinate reconstruction [4].

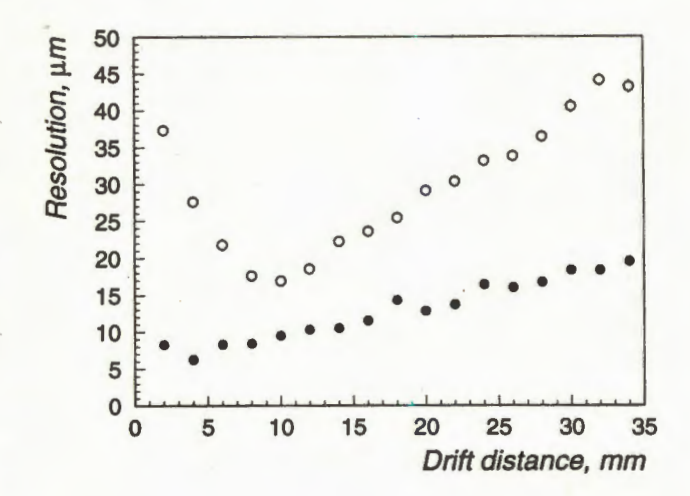


Fig.2. Coordinate resolution of the SDDs with a correlated noise as a function of the drift distance: white circles — r— $\phi$ -direction, black circles — drift direction

#### 4. dE/dx-Measurements in Silicon Detectors

Measurements of energy losses in silicon detectors can contribute to particle identification in the non-relativistic region. Moreover, for low-momentum tracks which do not reach the outer detectors the silicon tracker will be an independent particle spectrometer. Its dE/dx-resolution is discussed below. (We considred the pixel detector as a digital device and did not include it in dE/dx analysis).

Figure 3 shows distributions of ionization losses in the silicon detectors for muons with momenta of 5 GeV/c and normal angle of incidence without noise added. The results obtained are very close to those in LoI [2] and confirm estimates that dE/dx-measurements in the silicon tracker will be able to provide sufficient separation in the regions p < 1000 MeV/c  $(e/\pi)$ , p < 520 MeV/c  $(\pi/K)$  and p < 1 GeV/c (K/p), where «sufficient» means rejection factor of 100 at 95% efficiency. However, the electronics' noise can make the dE/dx-resolution worse as shown in Fig.4 for the SDDs and microstrip. One can see that the SDD response is affected significantly due to the fact that some part of the collected charge does not exceed the threshold and the fraction of the lost charge is not constant for all signals.

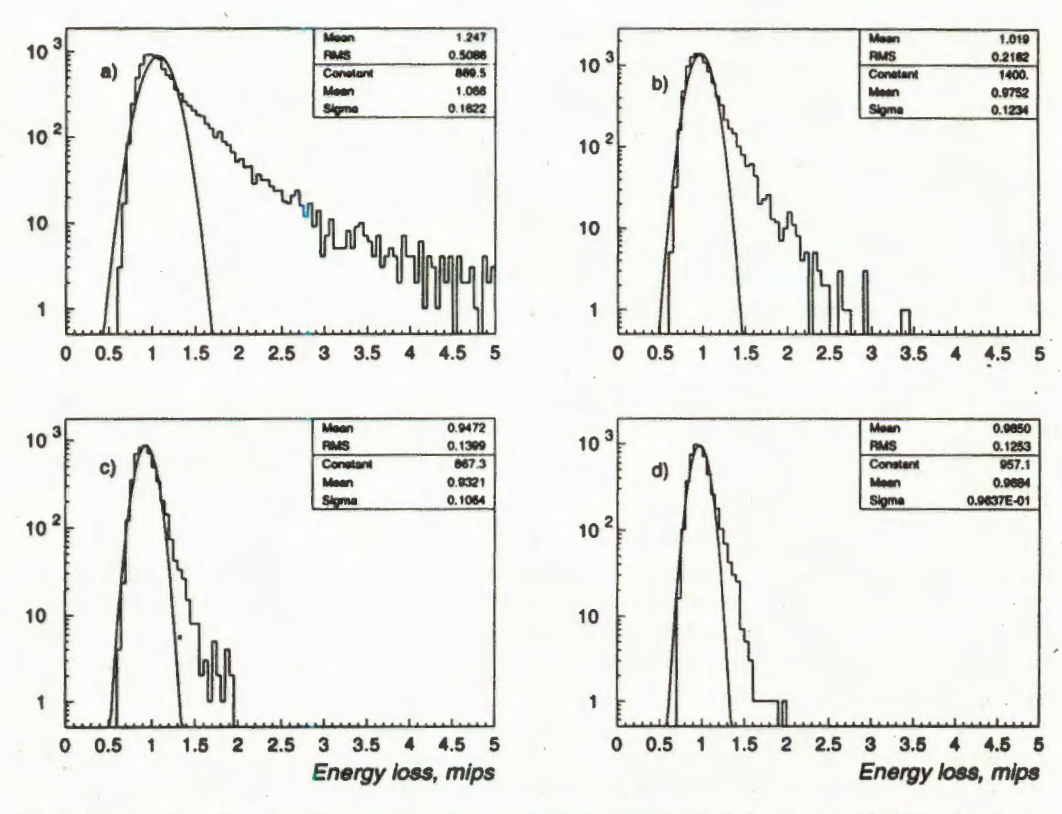


Fig. 3. Energy  $_{\rm s}$  loss distributions in silicon detectors, normalized to 1 at the most probable value. The parameters of a gaussian fit (full lines) around the most probable value are shown in the plots. a) Single detector response to minimum ionizing particle. b-d) Truncated mean using the m lowest of n measurements (b: one of two, c: one of three, d: two of four)

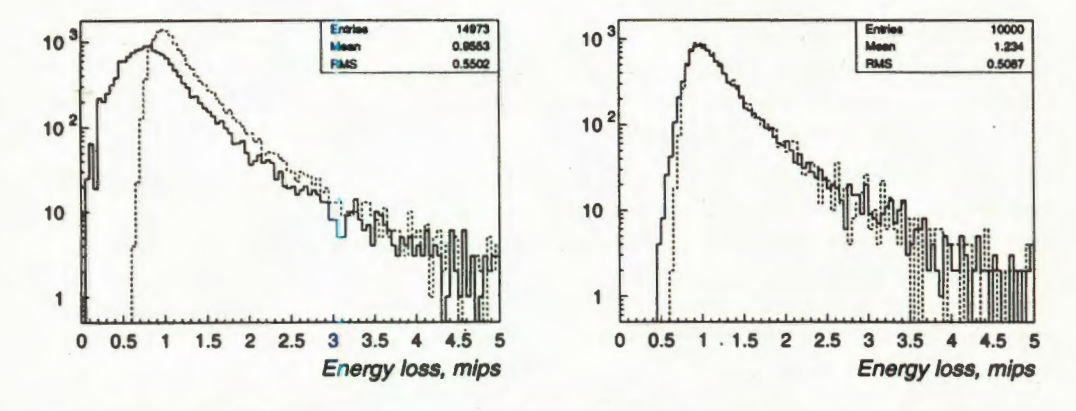


Fig.4. Energy loss distributions in the silicon drift detectors (left) and microstrip (right). Full line — with noise contribution, dashed line — without noise

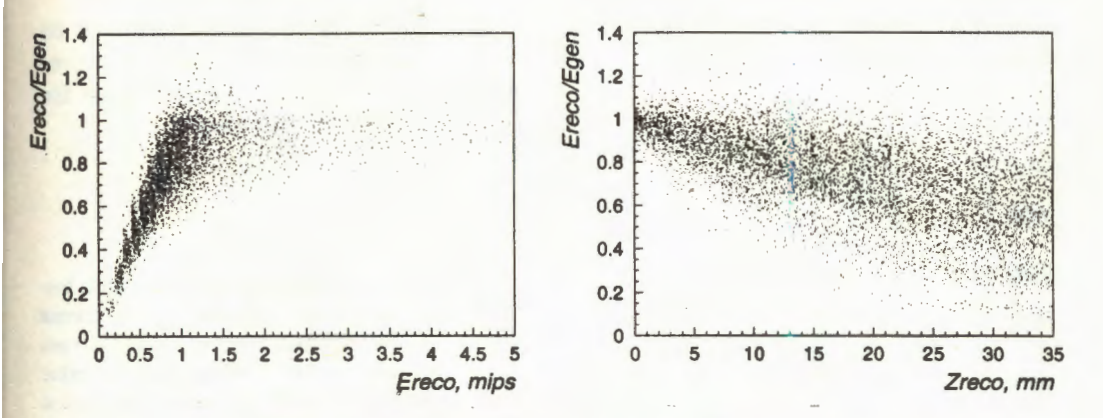


Fig. 5.  $E_{\text{reco}}/E_{\text{gen}}$  vs  $E_{\text{reco}}$  (left) and  $E_{\text{reco}}/E_{\text{gen}}$  vs  $z_{\text{reco}}$  (right) for 5 GeV/c muons with normal angle of incidence

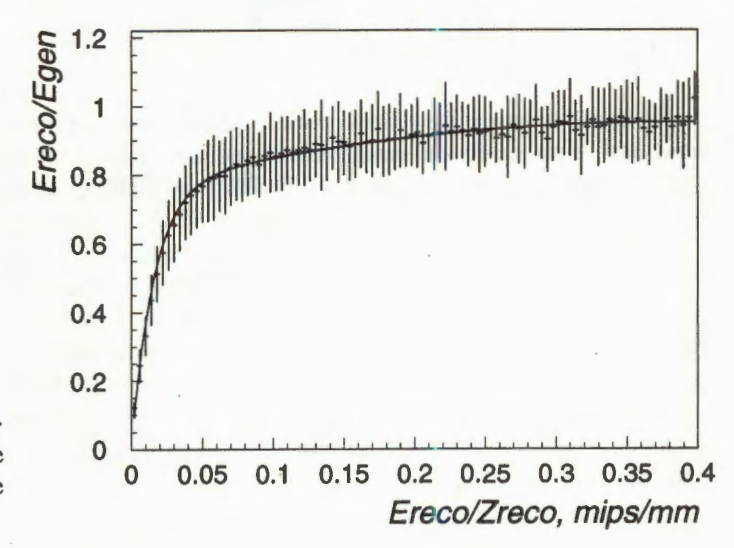
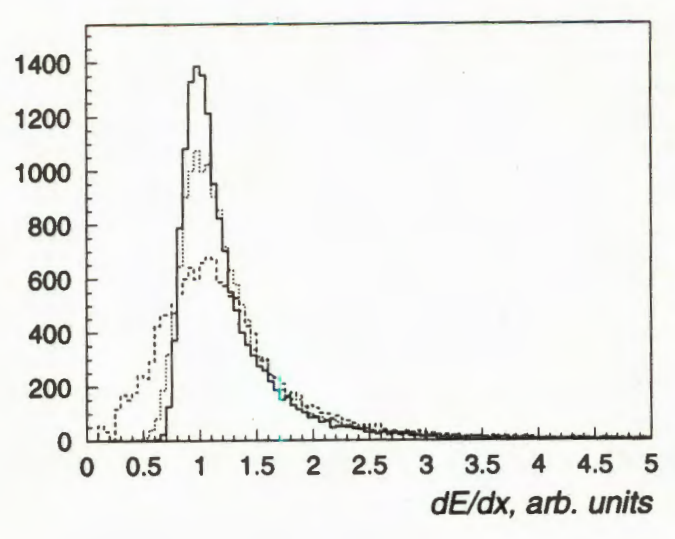


Fig.6.  $E_{\text{reco}}/E_{\text{gen}}$  vs  $E_{\text{reco}}/z_{\text{reco}}$ . The curve shows the result of the fit which was used to correct the detector response

One can try to restore the SDD resolution by introducing corrections. It looks reasonable to assume that the fraction of the lost charge is larger for small signals and long drift distances as can be seen in Fig.5 where a ratio of signals with noise added to those without noise  $(E_{\rm reco}/E_{\rm gen})$  is shown as a function of the signal  $(E_{\rm reco})$  and the drift distance  $(z_{\rm reco})$ . We combined these functions into one (Fig.6) and used it to correct the detector response. Figure 7 shows that this procedure works and helps to restore the dE/dx-resolution in the SDDs (at least, partially). After the correction we obtain the rejection factor of 100 at the following efficiencies; 94% ( $e/\pi$  and  $\pi/K$ ) and 82% (K/p), whereas without the correction results are significantly worse: 81%, 83% and 65%, respectively.



In conclusion it should be noted that this correction procedure might be useful also for gas drift chambers.

Fig.7. Distribution of ionization losses in the SDDs for 5 GeV/c muons with normal angle of incidence, normalized to 1 at the most probable value: solid line — without noise added, dashed line — with noise before correction, dotted line — after correction

#### 5. Multitrack Response

In order to study the silicon tracker capabilities in a multitrack environment we simulated one event of Pb-Pb central collisions with energy of 6.3 TeV/nucleon and charged particle density dN/dy = 5000 at y = 0 using the HIJING-package [5]. Figure 8 shows lego plots of what we can expect to see from the SDDs in the experiment.

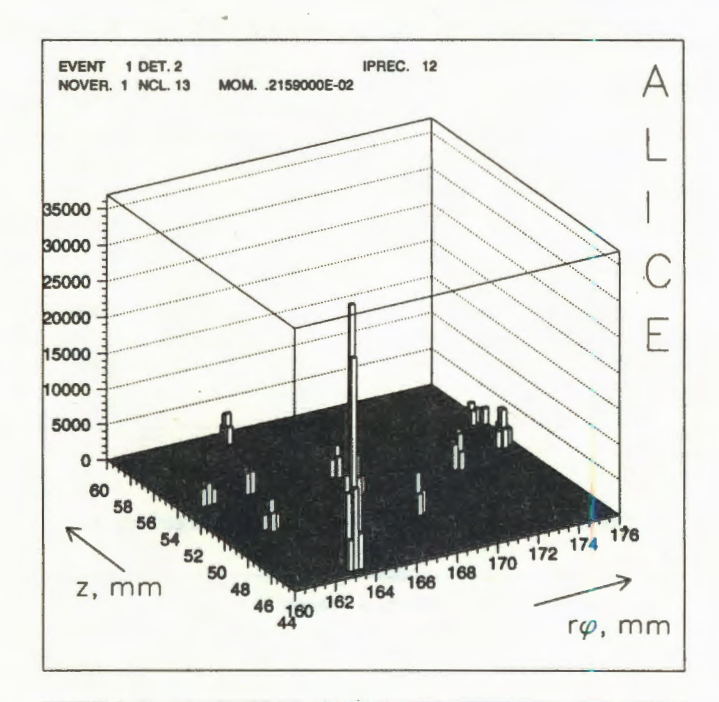
Table 1 shows a distribution of the number of primary charged tracks with  $\theta = 50^{\circ} + 90^{\circ}$  and momenta greater than 30 MeV/c producing a single cluster. Table 2 is similar to 1 except that all secondary charged tracks produced in the silicon tracker and beam pipe are taken into account. Table 3 is the same as 2 in configuration with additional passive material (support structure and cooling system) included as described in [6].

From a comparison of the tables we can see that the probability for signals from several tracks to overlap is low enough and extra material does not cause very serious problems from the point of view of particle interactions.

Another possible problem is a «ghost» activity in double-sided microstrip detectors with stereo angle. If the distance in r- $\phi$ -direction between two tracks traversing a detector is smaller than some value (1.5 mm in our case), then fake («ghost») hits appear. We found the average number of «ghost» hits per a real one to be equal to 0.18. This value is not significant and can be further reduced using a correlation of signals from two sides of the microstrip detector [7].

Thus, the current silicon tracker design seems to be adequate for the expected experimental conditions from the point of view of its granularity.

This can be further confirmed by the results on coordinate resolution. Distributions of generated and reconstructed coordinates for all charged tracks with momenta > 30 MeV/c are shown in Fig.9. The results shown are consistent with (and close to) the ones for single tracks [1] if the noise correlation in the SDDs (see section 3) and lower average  $\theta$ -angle



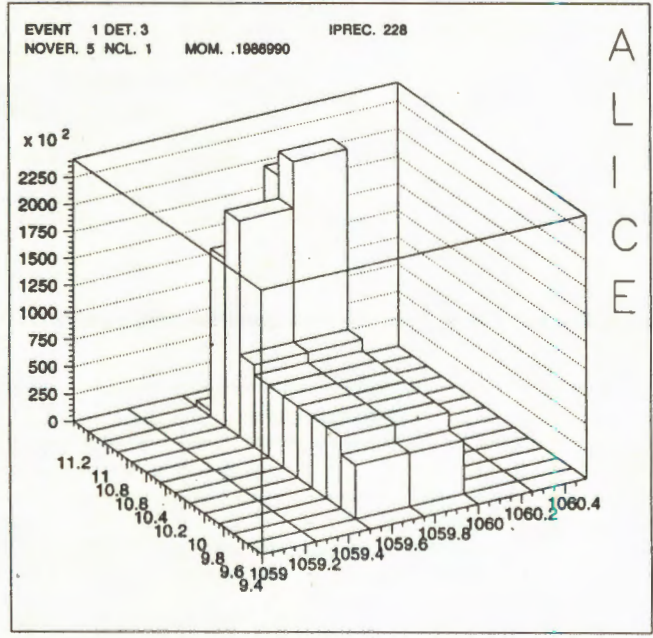


Fig.8. Lego plot of the silicon drift detector response (SDD # 1) to tracks with  $\theta \approx 70^{\circ}$  (top); plot showing a cluster produced by 6 close tracks (bottom)

Table 1. Number of primary charged tracks with  $\theta = 50^{\circ} + 90^{\circ}$  forming a cluster

Detector		Tracks/layer				
	1	2	3	> 3	mean	Tracks/rayer
pixel	3711	41	_	_	1.011	3793
SDD-1	3594	80	2	_	1.023	3760
SDD-2	3654	35	_	-	1.009	3724
SDD-3	3623	8	- '	-	1.002	3639
microstrip	3437	86	5		1.027	3624

Table 2. The same as in Table 1 for all charged tracks

Detector	Tracks per cluster								
	1	2	3	4	5	6	> 6	mean	- Tracks/layer
pixel	3815	54	1	2	1	1	-	1.018	3945
SDD-1	3736	98	3	_	_	_	_	1.027	3941
SDD-2	3854	46	1	1	1	_	1	1.016	3965
SDD-3	3937	18	2	1	_	_	1	1.008	3990
microstrip	3767	119	5	. –	_	2	_	1.036	4032

Table 3. The same as in Table 2 in configuration with passive material

Detector	Tracks per cluster								
	1	2	3	4	5	6	>6	mean	- Tracks/layer
pixel	3800	52	2	2	1	_	_	1.017	3923
SDD-1	3748	101	5	_		_	_	1.029	3965
SDD-2	3867	58	2	1	2	_	2	1.025	4029
SDD-3	4006	27	_	1	-	_	_	1.007	4064
microstrip	3845	116	6	1	_	_	- 2	1.037	4118

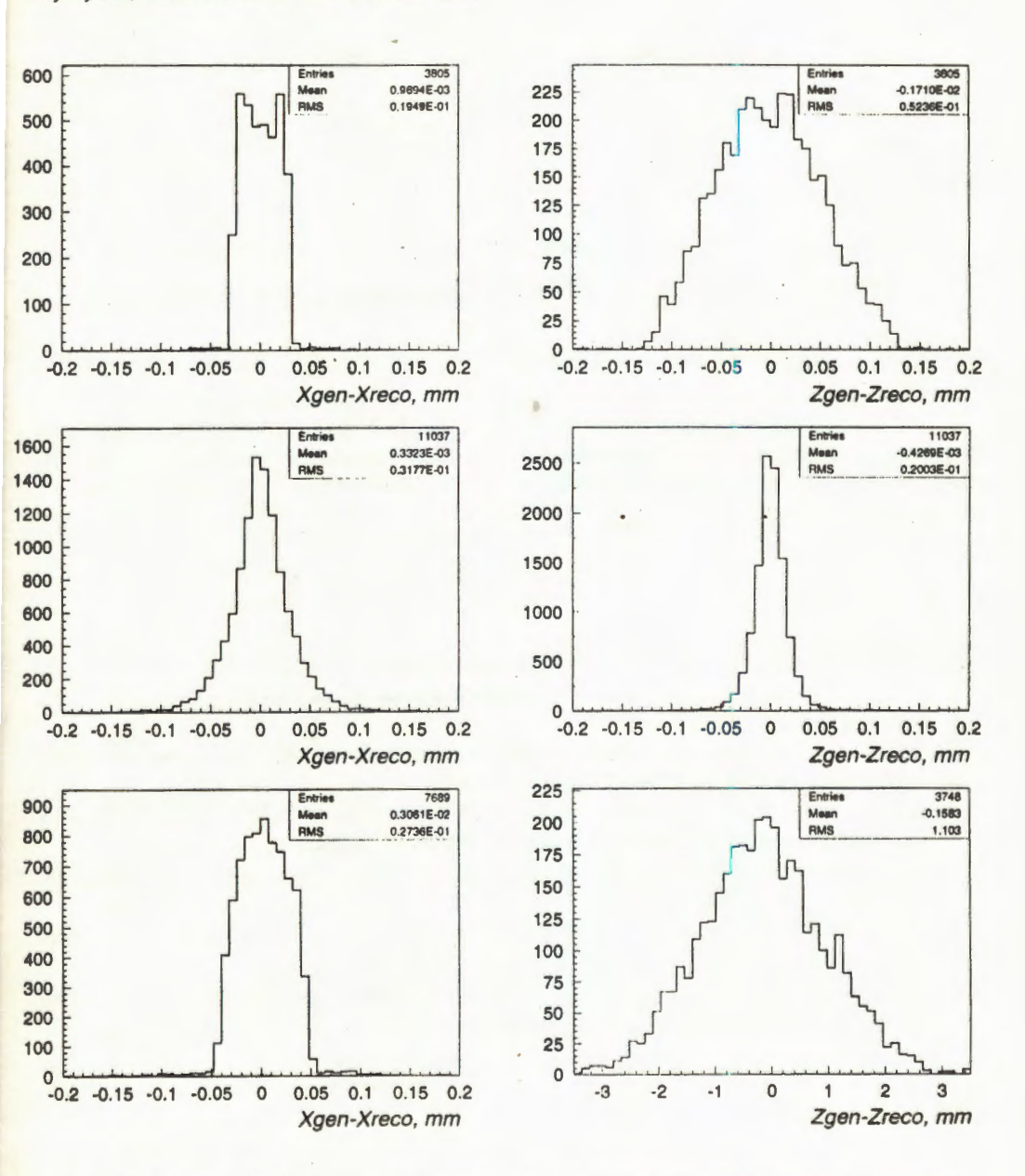


Fig. 9. Distributions of the difference of generated and reconstructed coordinates: upper — row-pixel, middle — SDDs, lower — microstrip; left column — r- $\phi$ -coordinate, right — z-coordinate

(which results in better z-coordinate resolution for the pixel detector) are taken into account. The average cluster size values are shown in Table 4. They are somewhat larger than the ones for single tracks.

Table 4. Average cluster size values for the silicon detectors

	Cluster size				
Detector	r	z-coordinate			
pixel	1.3 (pixels)	1.4 (pixels)			
SDD	2.0 (anode pads)	3.0 (FADC bins)			
microstrip	1.3 (strips)				

#### 6. Conclusion

The results of the «realistic» simulation of the ALICE silicon tracker performance presented here and in Ref. [1] confirm, in general, conclusions of the LoI [2]. However, they also indicate some problems which have to be addressed in order to reach designed parameters.

#### References

- 1. Batyunya B., Zinchenko A. JINR Communication, E1-94-375, Dubna, 1994.
- Letter of Intent for a Large Ion Collider Experiment, CERN/LHCC/93-16, LHCC/14, March 1993.
- Dabrowski W., Idzik M. Second-Order Effects in Front-End Electronics and APSP Robustness, Note RD20/TN/15, March 1993.
- Kozlowski M. et al. The Resolution of the Linear Silicon Drift Detector Studied by a Computational Model, Internal Note ALICE/94-10, 1994.
- Wang N.X. et al. Phys. Rev., 1991, D44, p.3521; Phys. Rev. Lett., 1992, 68, p.1480.
- Godisov O.N. et al. Evaporative Cooling for the ALICE Inner Tracker: First Prototype Tests, In: Internal Note ALICE /93-36, November 1993.
- Monteno M. Study of the Efficiency of Charge-Matching Methods to Solve Ambiguous Tracks in 2-Sided Silicon Detectors, Internal Note ALICE/94-13

УДК 539.124.122

# A STUDY OF SINGLE TAGGED MULTIHADRONIC $\gamma\gamma^*$ EVENTS AT AN AVERAGE $Q^2$ OF 90 GeV<sup>2</sup>

B.Batyunya, J.Bjarne<sup>1</sup>, F.Kapusta<sup>2</sup>, V.Pozdnyakov, I.Tyapkin, N.Zimin

A selection of multihadronic two-photon events has been performed in the single tagged mode using the forward electromagnetic calorimeter. The  $60.6 \ pb^{-1}$  integrated luminosity data was compared to a two-component model prediction: a Quark Parton Model (QPM) describing the point-like photon-quark coupling and a Generalized Vector meson Dominance Model (GVDM) for the hadron-like part. The agreement between the data and the simulation is satisfactory to measure the photon structure function  $F_2^{\gamma}(x, Q^2)$  and to check a QCD prediction on the  $Q^2$  evolution of the photon structure function.

The investigation has been performed at the Laboratory of High Energies, JINR.

# Изучение меченых мультиадронных $\gamma \gamma^*$ -событий при $\langle Q^2 \rangle \cong 90$ ГэВ $^2$

## Б.Батюня и др.

Мультиадронные двухфотонные события были отобраны в моде одиночного мечения при использовании переднего электромагнитного калориметра. Экспериментальные данные, соответствующие интегральной светимости  $60.6~\rm nG^{-1}$ , сравниваются с предсказаниями двухкомпонентной модели — кварк-партоиной модели и обобщенной модели векториой доминантности для описания, соответствению, точечноподобного и адроноподобного процессов расщепления фотоиа. Получено удовлетворительное согласие предсказания модели с экспериментальными данными для последующего измерения структурной функции фотона и проверки предсказаний КХД о  $Q^2$  эволюции структурной функции.

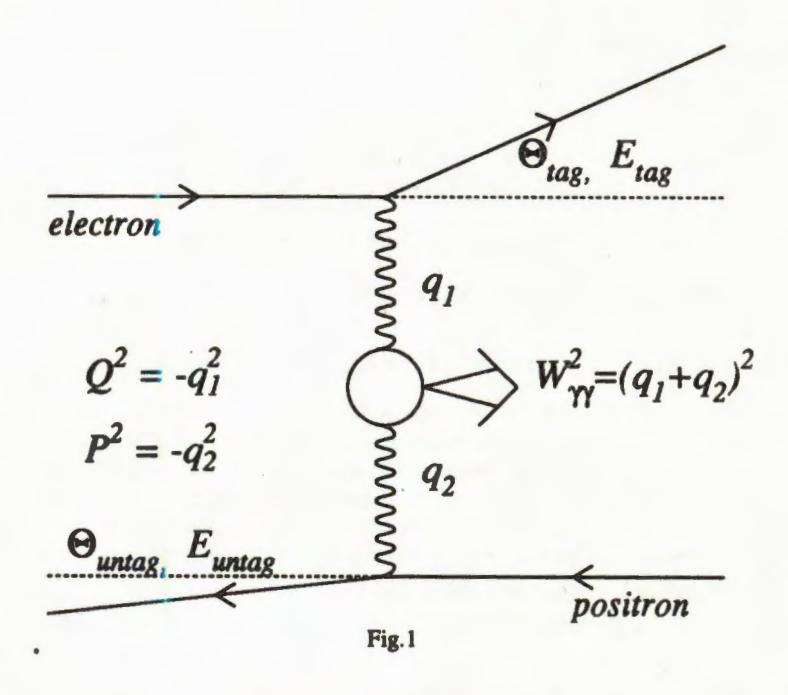
Работа выполнена в Лаборатории высоких энергий ОИЯИ.

#### 1. Introduction

In the reaction  $e^+e^- \to e^+e^- X$ , where X is a multihadronic system produced by the collision of two virtual photons coming from the beam particles, one of the scattered leptons can be detected. Its energy  $E_{\text{tag}}$  and scattering angle  $\theta_{\text{tag}}$  can be measured (figure 1),

<sup>&</sup>lt;sup>1</sup>Dept. of Physics, University of Lund, Sweden

<sup>&</sup>lt;sup>2</sup>LPNHE, IN2P3-CNRS and Universities Paris VI and VII, France



thus giving the virtual photon squared mass through  $-Q^2 = -4E_{\text{tag}}E_b \sin^2(\theta_{\text{tag}}/2)$ , where  $E_b$  is the beam energy. In these «single tag» events the other photon can be required to be almost on-shell and the whole process is viewed as deep inelastic scattering of an electron off a quasi-real photon with a squared mass  $-P^2 \cong 0$ .

The corresponding cross section reads:

$$\frac{d\sigma}{dE_{\text{tag}}d\cos(\theta_{\text{tag}})} = \frac{4\pi \alpha^2 E_{\text{tag}}}{Q^4 y} \left[ (1 + (1 - y)^2) F_2^{\gamma}(x, Q^2) - y^2 F_L(x, Q^2) \right]$$
(1)

with

$$y = 1 - E_{\text{tag}} / E_b \cos^2(\theta_{\text{tag}} / 2),$$
  
$$x = \frac{Q^2}{Q^2 + W_{\text{ty}}^2}.$$

 $F_2(x, Q^2)$  and  $F_L(x, Q^2)$  structure functions are defined in terms of cross sections for photons with different helicities (for details see [1]).  $W_{\gamma\gamma}$  is the invariant mass of produced hadron system.

Only a few previous experiments have studied the photon structure function  $F_2^{\gamma}$  at  $Q^2$  greater than 50 GeV<sup>2</sup> [2,3,4]. Using the DELPHI detector a new measurement of  $F_2^{\gamma}$  can be obtained. The detailed description of the detector can be found elsewhere [5]. Experimentally, a scattered lepton can be tagged in the Forward ElectroMagnetic Calorimeter (FEMC) at relatively large angles ( $10^{\circ} \le \theta_{\text{tag}} \le 36.5^{\circ}$ ). Using estimates for  $F_2^{\gamma}$  and  $F_L$  in the Quark Parton Model [1], and taking into account that  $\langle y \rangle \cong 0.15$  under experimental conditions, it was found that the cross-section of the process is saturated by the structure function  $F_2^{\gamma}$  only.

The theoretical background of the photon structure function can be found elsewhere [6,7]. Section 2 describes the data selection, while the two-component model used here is described in section 3. The background subtraction is discussed in section 4. Finally, in section 5 are the results and a comparison with a two-component model presented.

#### 2. Event Selection

Since there is about two radiation lengths of materia in front of FEMC a specific algorithm was used to determine the tagged particle energy. The largest cluster in each FEMC arm was found. Smaller clusters, but with energies greater than 0.5 GeV, were then added if their distances to the largest cluster were smaller than 30 cm in the  $R\phi$  plane. The

values were found based on  $e^+e^-$  events detected in FEMC. We will call this final cluster a «summed cluster». The kinematic characteristics of the summed cluster are thus determined by the summed clusters barycenter, where a weight of each cluster component was proportional to its energy. The comparison of the distribution for the distance for the data and the simulation described below is shown on figure 2.

Events were accepted if there was a summed cluster (tagged cluster) with energy greater than 30 GeV in one FEMC arm and no summed cluster with energy greater than 15 GeV in the other arm.

The following selection criteria were used:

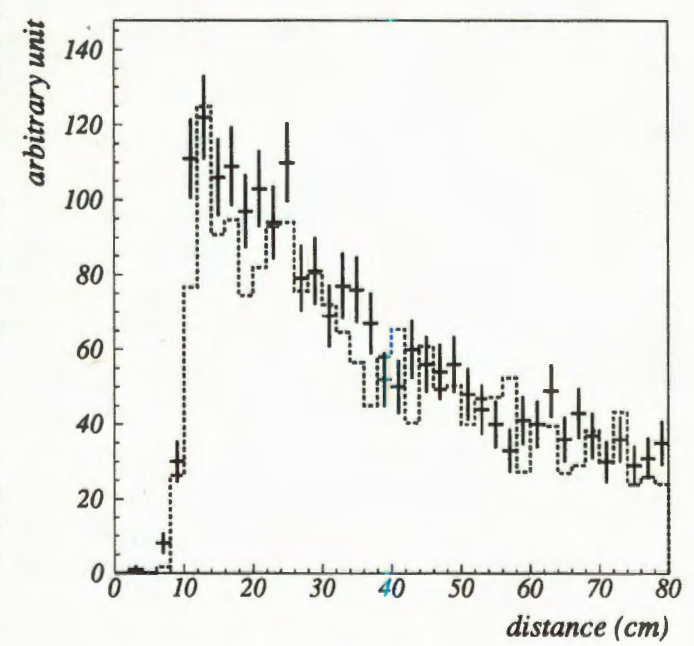


Fig.2

- At least 3 charged tracks having momentum greater than 0.4 GeV and polar angles θ between 20° and 160° were required. The relative error on the momentum had to be less than 100%, while the impact parameter had to be smaller than 4 cm in Rφ and 10 cm in z:
- Neutral particles were required to deposit at least 1.0 GeV in the barrel electromagnetic calorimeter High-density Projection Chamber (HPC) or 0.5 GeV in FEMC:
- To avoid the region of the two-photon resonance production and problems with the Monte Carlo fragmentation reliability, the invariant mass of the system (excluding tagged cluster) was required to be greater than 2.0 GeV;
- The thrust (excluding the tagged cluster) was required to be smaller than 0.99 in order to reject photon conversion events as well as contaminations from τ<sup>+</sup>τ<sup>-</sup> pairs.

After the preselection there are 367, 1166 and 1087 events for the 1991, 1992 and 1993 runs, respectively. It was checked that there was no essential disagreement between the different year data. The data was united into one sample. Since the threshold for trigger  $\gamma$  in FEMC is 25 GeV, the requirement of the large energy cluster in FEMC makes us sure that the efficiency to trigger events is close to 100%.

#### 3. Monte Carlo Simulation

A two-component model was used for the  $\gamma\gamma$  event simulation. QPM describes a perturbative term of the process where a photon splits into a quark pair (the point-like term). The non-perturbative part describing a bound state in the photon quark coupling (the hadron-like term) was introduced through GVDM [8]. The GVDM multihadronic final system was generated as a  $q\bar{q}$  system according to a distribution of the transverse momentum of the quark in the  $\gamma\gamma$  center-of-mass system quark  $(d\sigma/dp_T^2 \equiv \exp{(-5p_T^2)})$ . The TWOGAM  $\gamma\gamma$  event generator [9] was used with default parameters, while the JETSET 7.3 string fragmentation scheme was used for the fragmentation of the produced quarks.

Measurements at PEP and PETRA have shown that for  $Q^2$  values greater than 20 GeV<sup>2</sup> the point-like coupling part dominates the cross section of the  $\gamma\gamma^*$  process. The following table gives the cross sections  $\sigma_{\text{tot}}$  when one of the scattered leptons is within the angular range of FEMC. The cross section  $\sigma_{\text{expect}}$  is after detector simulation and selection procedure introduced above. The large decrease of the cross section is due to the cuts applied to the hadron system.

cross section in pb	GVDM	QPM
σ <sub>tot</sub>	9.4	12.6
of expect	0.5	1.5

#### 4. Background Rejection

The expected number of two-photon events (around 100) is small compared with powerful  $Z^0$  background. To determine criteria in order to extract  $\gamma\gamma$  events, one needs to make sure that the data and  $Z^0$  Monte Carlo simulation are in agreement. Around 900000  $Z^0$  simulated hadronic events ( $\cong 30 \text{pb}^{-1}$ ) were processed taking into account the selection criteria. Also Monte Carlo simulation of other sources of a background was considered. The contribution of  $e^+e^-$  events in the sample was evaluated to be around  $11\pm 5.5$  events,  $Z^0 \to \tau^+\tau^-$  gives  $6.3\pm 1.8$  events,  $\gamma\gamma^+ \to \tau^+\tau^-$  gives  $8\pm 3$  events. Figures 3(a,b) show energy and polar angle distributions for the tagged cluster. A charged multiplicity and invariant mass calculated using charged and neutral component distributions of hadron system are

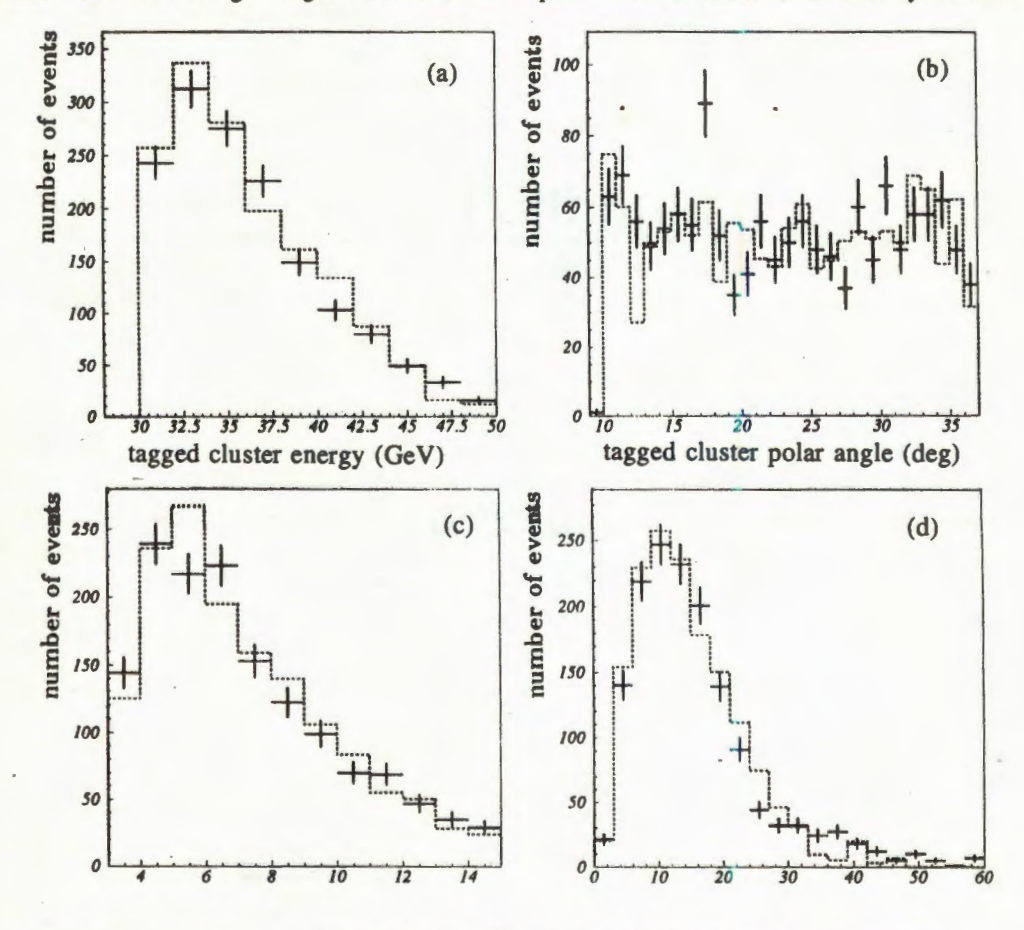


Fig. 3. The comparison of the distributions for the data (bars) and Monte Carlo simulation (histograms): tagged cluster energy (a); tagged cluster polar angle (b); charged multiplicity in the event (c); invariant mass of the hadron system calculated using charged particles and neutrals measured in the electromagnetic calorimeters (d)

shown in figure 3(c,d), respectively. All distributions are compared to the  $Z^0$  simulated events together with  $\gamma\gamma$  simulation. The agreement is reasonable to choose for criteria to extract two-photon events based on Monte Carlo.

Let us introduced two dimensionless variables: Normalized Longitudinal Momentum Balance

$$NLMB = \text{sign } (p_z^{\text{tag}}) + \sum_i p_z^{i, \text{ hadron}} \\ \frac{E_{\text{beam}}}{E_{\text{beam}}},$$
 (2)

and Normalized Transverse Momentum Balance

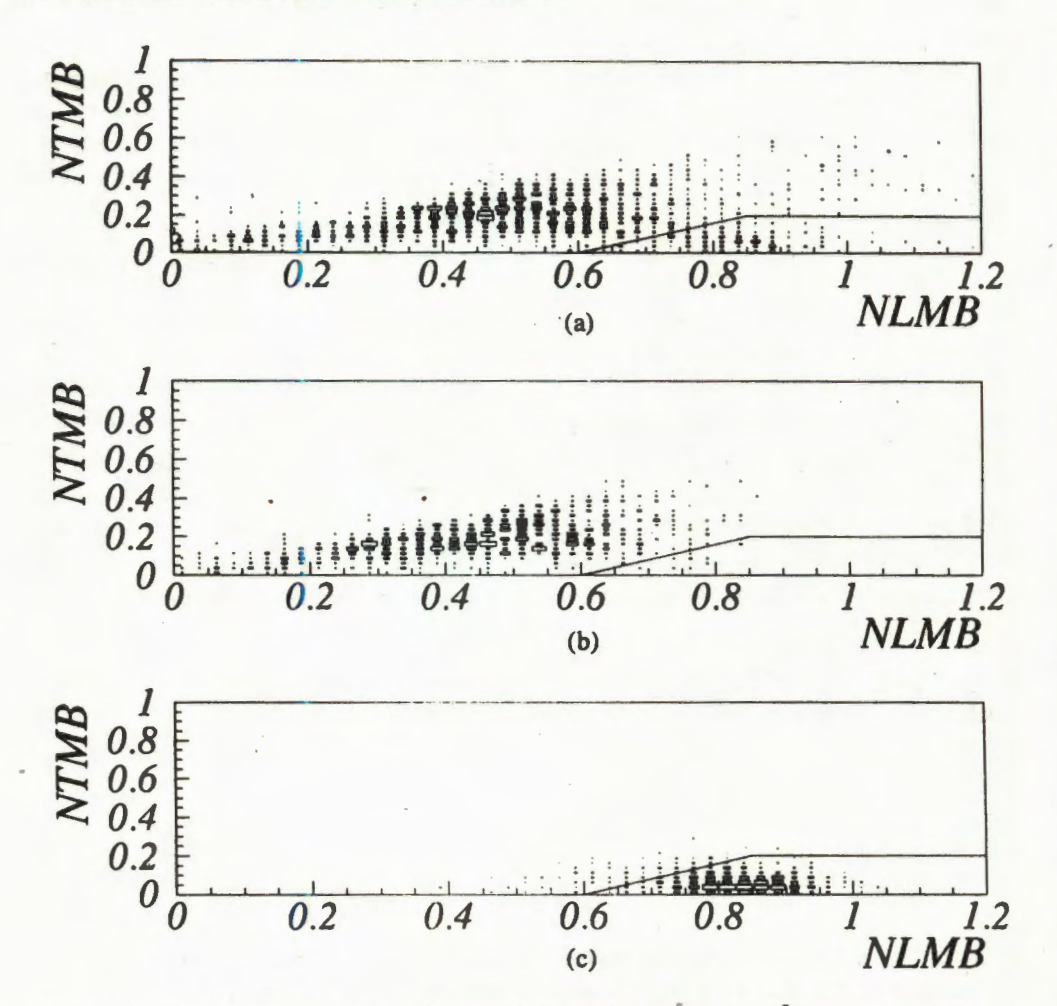


Fig. 4. The correlation plots between NLMB and NTMB for the data (a),  $Z^0$  (b) and  $\gamma\gamma$  (c) Monte Carlo simulation

$$NTMB = \frac{\parallel \mathbf{p}_{T, \text{ tag}} + \sum_{i} \mathbf{p}_{T}^{i, \text{ hadron}} \parallel}{E_{\text{beam}}}, \tag{3}$$

For the events with a few lost particles both the first variable and the second one express the fact that the longitudinal and transverse momentum are balanced. Besides from that at least one scattered lepton (most probable with a small transverse momentum) is undetected in two-photon single tagged mode. The main consequence is an expected unbalance in longitudinal direction for two-photon events.

Figures 4(a—c) show the NLMB vs NTMB for the data,  $Z^0$  and two-photon Monte Carlo, respectively. It is seen that the main part of  $Z^0$  background is concentrated below 0.6 NLMB. The two-dimensional cut was used:

• NTMB  $\leq$  0.2 and the domain above the line connecting the point (0.6, 0.0) and (0.85, 0.2) was rejected (solid line in figures 4).

To suppress the remaining background the following cuts were added:

- · the sum of charged particle momentum in the event was lower than 20 GeV;
- the polar angle of the tagged cluster was below 17 degree. Figure 3b shows that the polar angle distribution for a tagged cluster for Z<sup>0</sup> events has a uniform behaviour. Besides from that two-photon events are peaked at the small polar angle domain. The upper limit of the polar angle domain for the tagged cluster allows to remove many Z<sup>0</sup> events saving most part of γγ events;
- there is no particle detected in the luminosity monitor [5] with the energy greater than 20 GeV («antitagging condition»).

After applying the cuts above we are left with 123 events with the background from  $Z^0$  of 9.4±3.9 events. The other sources of a background like  $\tau$  pair production (both in two-photon and annihilation reactions), Bhabha events and beam-gas interactions were estimated as negligible.

The main features of a single tagged event can be seen on the  $R\varphi$  and Rz projections (figure 5) for one selected event. The track detectors and electromagnetic calorimeters are drawn. The showers in calorimeters are drawn by boxes. The solid lines show reconstructed charged particles, the dashed show neutrals. It is seen a separate cluster in FEMC produced due to a shower before FEMC.

The features described below are consequence of the fact that both an energy and a polar angle of emitted photons are peaked at small values. Thus most probable that produced quarks (hadrons) are boosted in direction z of a target particle if its energy is small compared to the beam energy (the normalized longitudinal momentum balance NLMB introduced above is the quantitative description of such feature). The reconstructed energy of the tagged electron was 37.4 GeV for the selected event. It is seen on the Rz projection that the main part of produced hadrons move in positive z direction as the tagged electron. On the  $R\varphi$  projection one can see that the produced hadrons move in the direction opposite to the tagged particle, since a polar angle of the untagged scattered lepton is peaked at small values.

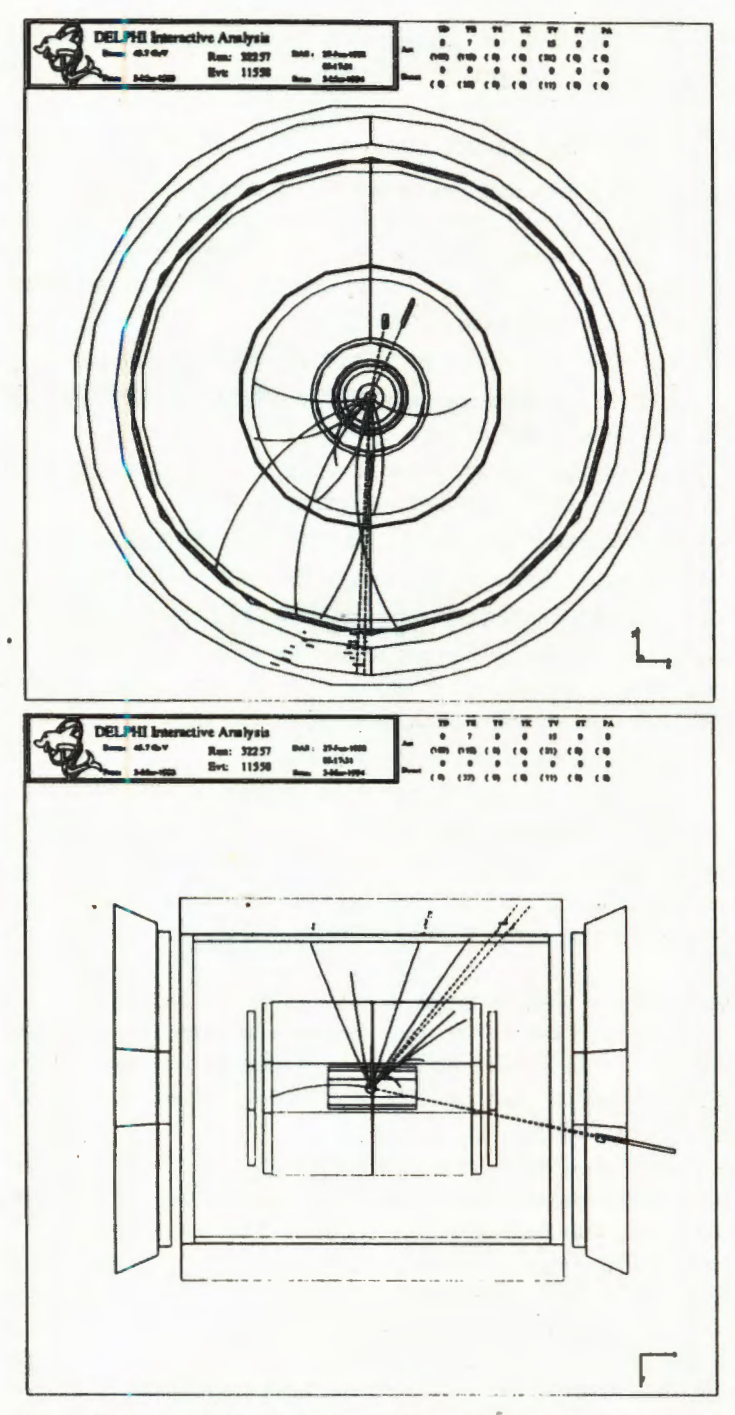


Fig. 5.  $R\varphi$  (upper plot) and Rz (lower plot) projections of one selected event

#### 5. Result and Conclusion

Two photon events tagged in FEMC can be selected with less than 10% background. They are in qualitative agreement with the sum of two models: QPM and GVDM describing the point-like and bound state behaviours of the photon to quark coupling. Figures 6(a-d) show the charged invariant, multiplicity mass,  $Q^2$  and x distributions respectively for the data compared to QPM plus GVDM Monte Carlo predictions.

The squared mass of the virtual photon obtained from the measurement of the energy and the polar angle of the scattered lepton in FEMC varied from  $40 \text{ GeV}^2$  to  $200 \text{ GeV}^2$  with an average of  $90 \text{ GeV}^2$ .

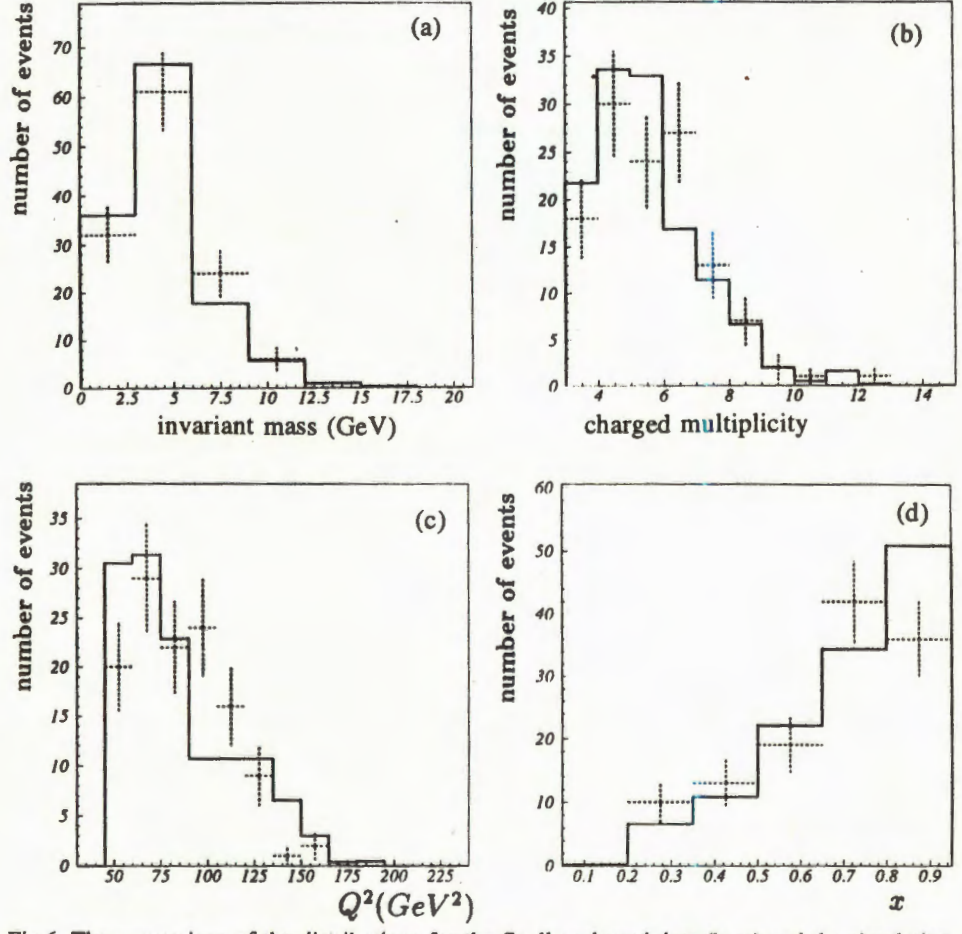


Fig.6. The comparison of the distributions for the finally selected data (bars) and the simulation (histograms): invariant mass of the hadron system (a); charged multiplicity in the event (b);  $Q^2$  (c) and x (d)

Theory predicts specific features for the behaviour of  $F_2^{\gamma}(x,Q^2)$ . The calculations have shown that the photon structure function increases with x. The  $Q^2$  dependence of  $F_2^{\gamma}$  in the restricted x domain was found to be proportional to  $\ln \langle Q^2 \rangle$  [1]. The test of these QCD predictions should proceed through  $F_2^{\gamma}$  unfolding [10] to take into account the effect of limited acceptance and finite resolution of the detector.

#### References

- 1. Budnev V.M. et al. Phys. Rep., 1975, 15C, p.
- 2. PLUTO Collab., Berger Ch. et al. Phys. Lett., 1987, B281, p.365.
- 3. JADE Collab., Bartel W. et al. Z. Phys., 1984, C 24, p.231.
- 4. AMY Collab., Sasaki T. et al. Phys. Lett., 1990, B 252, p.491.
- 5. DELPHI Collab., Aarnio P. et al. NIM, 1991, A 303, p.233.
- 6. Berger Ch., Wagner W. Phys. Rep., 1987, 146, p.1 and references therein.
- 7. Batyunya B. et al. DELPHI note 93-60, 1993.
- 8. Peterson C., Walsh T.F., Zerwas P. Nucl. Phys., 1983, B229, p.301.
- 9. Nova S., Olshevski A., Todorov T. DELPHI note 90-35, 1990.
- 10. Blobel V., Cern School of Computing, Aiguablava, Spain (1984), CERN 85-09.

УДК 621.039.573

# EPITHERMAL NEUTRON ACTIVATION ANALYSIS OF MOSS, LICHEN AND PINE NEEDLES IN ATMOSPHERIC DEPOSITION MONITORING

V.M.Nazarov, M.V.Frontasyeva, V.F.Peresedov, V.P.Chinaeva, T.M.Ostrovnaya, S.F.Gundorina, V.V.Nikonov\*, N.V.Loukina\*

Experience in the use of epithermal neutron activation analysis (ENAA) in the monitoring atmospheric deposition by means of moss, lichens and pine needles is summarized. It is shown that 45 elements (Mg, K, Ca, Al, Cl, Sc, V, Cr, Mn, Fe, Co, Ni (using (n, p)-reaction), Zn, Cu, As, Se, Br, Rb, Sr, Zr, Mo, Ag, Sn, Sb, I, Cs, Ba, La, Ce, Nd, Sm, Eu, Gd, Tb, Tm, Yb, Lu, Hf, Ta, W, Au, Th and U, as well as Ir and Re in pine needles in the presence of anthropogenic pollution by the nickel smelter complex) are reliably determined. Examples of the use of lichens, moss and pine needles as biomonitors of atmospheric deposition in Franz Josef Land, the Kola Peninsula and in the Tver region are given.

The investigation has been performed at the Frank Laboratory of Neutron Physics, JINR.

Эпитепловой нейтронный активационный анализ мхов, лишайников и хвон сосны в мониторинге атмосферных выпадений

## В.М.Назаров и др.

В настоящей работе обобщается опыт эпитеплового нейтронного активационного анализа (ЭНАА) биомониторов (мох, лишайники, хвоя сосны), используемых для мониторинга атмосферных выпадений. Показано, что этим методом могут быть достоверно определены 45 элементов (Mg, K, Ca, Al, Cl, Sc, V, Cr, Mn, Fe, Co, Ni (используя (n, p)-реакцию), Zn, Cu, As, Se, Br, Rb, Sr, Zr, Mo, Ag, Sn, Sb, I, Cs, Ba, La, Ce, Nd, Sm, Eu, Gd, Tb, Tm, Yb, Lu, Hf, Ta, W, Au, Th и U, а также Ir и Re в хвое сосны при наличин антропогенных загрязнений окружающей среды никелеплавильным металлургическим комбинатом). Приводятся примеры использования лишайников, мхов и хвои сосны в качестве биомониторов атмосферных выпадений на Земле Франца-Иосифа, Кольском полуострове и Тверской области.

Работа выполнена в Лаборатории нейтронной физики ОИЯИ.

<sup>\*</sup>Institute of Industrial North Ecology Problems, Kola Scientific Centre of RAS, Apatity, Russia

#### Introduction

At present, in the practice of biomonitoring of atmospheric deposition of trace elements, moss, lichens, and pine needles are used as biomonitors. The Scandinavian countres, and especially Norway [1—3] have extensive experience in the use of moss for this purpose.

To determine the trace elements content, atomic absorption spectroscopy (AAS) in combination with INAA were frequently used. In the last few years inductively coupled plasma emission spectroscopy (ICP-ES) and inductively coupled plasma mass spectroscopy (ICP-MS) have been the chosen methods [4].

Experience in the use of NAA by means of thermal neutrons [4] shows that INAA of the moss Hylocomium splendens allows the determination of only 13 elements.

Our experience with the use of resonance neutrons in INAA of lichens from Franz Josef Land [5] showed that at the IBR-2 reactor 45 elements (Mg, K, Ca, Fe, Na, Cl, Mn, Se, Zn, Cu, V, Zr, Ti, Br, Y, Cr, I, Ni, Ba, Co, Sc, Rb, Sn, W, Mo, Se, As, Hf, Ag, Sb, Ta, Cs, Au, La, Ce, Nd, Sm, Eu, Tb, Ho, Tm, Yb, Lu) were reliably determined.

Thus, to extend the possibilities of using the IBR-2 reactor in analytical applications [6] the present investigations were carried out on the use of resonance neutrons for biomonitoring by means of moss, pine needles and lichens.

In the methodical investigations on the use of INAA for moss, lichens and pine needles analysis, moss samples from Norway [7] and pine needles samples from the Kola Peninsula and Tver region were utilized.

## Experiment

Reliable determination of the trace element content in pine needles is based on samples of *Pinus sylvestris L* collected in 11 points of Tver region from five one-year old trees growing in a square of about 100 sq.m. These 11 collection points are situated along the perimeter of approximately 3000 sq.km. In the same points the moss samples *Hylocomium splendens* were collected from the same square. Samples from 5 trees and 5 moss species were used for preparation of one averaged sample respectively to be analysed by INAA. Pine samples of the same type from the Kola Peninsula were collected from 7 trees.

Lichens were collected in the region of the Lunnik glacier on Alexandra Island (Franz Josef Land).

Moss, lichen and pine needle samples were airdried in the air and homogenized. Then 0.5 g samples were chosen and packed in Al cups for long-term irradiation and in polystyrene packs for 3—5 minute irradiation. Samples were irradiated in channels Ch1, Ch3 and Ch4 of the IBR-2 reactor. Densities (n / (cm $^2$ ·s)) of thermal ( $F_{\rm th}$ ), resonance ( $F_{\rm epi}$ ) and fast ( $F_{\rm fast}$ ) neutrons in these channels are given in Table 1.

Irradiation time for long-lived isotopes varied from 4 to 7 days in Ch.1 and was 10 days in Ch.3 and Ch.4. Decay time for the first measurement was 4—6 days, for the second one it was 20—30 days. Measuring time varied from 1 to 5 h.

Irradiation site	Neutron fl	ux density (n / (cm	T°,C	Chan.	Chan. length,	
	Thermal	Resonance	Fast	1,0	mm	mm
Ch.1	Cg coat	0.23 ± 0.03	1.4 ± 0.16	70	28	260
Ch.2	$0.54 \pm 0.06$	0.12 ± 0.014	$0.64 \pm 0.04$	60	28	260
Ch.3	Gd coat	0.9 ± 0.10	$7.0 \pm 0.5$	30-40	30	400
Ch.4	$13.0 \pm 0.5$	1.25 ± 0.1	$7.0 \pm 0.5$	30—40	30	400
Ch.0	no	< 0.1	150	400	16	180

Table 1. Characteristics of the irradiation channels at the IBR-2 reactor

To determine Cl, V, I, Mg, Cu, Al, and Mn, Ch.1, equipped with a pneumatic system, was used. Irradiation time  $T_i = 5$  min., decay time  $T_d = 3$ —5 min., counting time  $T_c = 5$ —8 min.

In the second measurement with  $T_{\rm d} = 15$  h, the concentrations of K and Na were determined from the same samples. Comparison of our results is made with data on moss reference material DK-1 [7].

Gamma spectra were measured using Ge(Li) detectors with a resolution of 2.5 keV for the <sup>60</sup>Co 1332.4 keV line, with an efficiency of about 6% compared to 3" × 3" NaI detector for the same gamma line. Data processing and element concentration determination was performed on the basis of standard reference materials and comparators, using software developed in FLNP JINR [8].

In irradiations of more than 3 days in Ch.1, a single comparator of Au (10<sup>-6</sup> g) was used. For 3—5 minutes of irradiation its concentration was (10<sup>-6</sup> g). For comparison with Ch.3, a comparator of Zr (9<sup>5</sup>Zr and 9<sup>7</sup>Zr) (10 mg) was used. Concentrations of elements which had long-lived isotopes were also determined using standard reference materials SDM, SL-1 (International Atomic Agency, Vienna) and DK-1 [7].

#### Results and Discussion

Element concentrations for moss reference material DK-1, lichens and pine needles with detection limits for pine needles are given in Tables 2 and 3. Detection limits for lichens and mosses are close to those in pine needles. Detection limits and element concentrations of anthropogenically polluted pine samples (Pechenga-Nickel), irradiated in Ch.1 and Ch.3, are shown in Fig.1.

Detection limits are significantly lower for Ch.3 with the exception of Cl, Cr, Nd, Tm, Gd, W. It can be seen from a comparison of results from Ch.1 and Ch.3 that the detection limits are only noticeably lower for Eu, Sc, Co, Lu, Hg, Cr, Fe, Na and U. This is understandable as these elements are characterized by low  $I_0 / \sigma_0$  and by the use of Gd coat.

Table 2. Element concentrations in moss samples Hylocomium splendens, lichen ones Usnea sp, pine needles Pinus sylvestris L, and the detection limits for pine needles as measured in irradiation channels 1 and 3

F1		Element concentrations, pm						
Element	Moss DK-1	Lichen Usnea sp	Pine needles	Concentr. limit	$\sigma_0$			
Na	530(8)	900(5)	121(5)	5.01	0.59			
Mg	< 800	8200(10)	2500(15)	600 <sup>1</sup>	0.68			
Al	480(5)	< 50	750(5)	20 <sup>1</sup>	0.74			
Cl	328(11)	57(20)	810(20)	100 <sup>1</sup>	0.69			
K	3300	1800(40)	5000(8)	190	0.97			
Ca	1630(3)	5100(46)	2500(35)	340	1.31			
Sc	0.16(13)	2.0(8)	0.043(15)	1.0E-3	0.44			
V	6.0(10)	17.0(6)	2.2(17)	0.61	0.55			
Cr	1.9(8)	3.2(8)	1.9(15)	0.1	0.53			
Mn	143(7)	53.0(4)	198(5)	3.51	1.07			
Fe	575(9)	2200(8)	194(17)	2.0	1.30			
Co	0.26(5)	2.23(7)	6.8(7)	5 OE-3	2.02			
Ni	1.58(21)	2.70(15)	190(5)	0.3	(n, p)			
Cu	240(25)	< 20	280(8)	25 <sup>1</sup>	1.06			
Zn	30.8(13)	21.4(5)	21.0(6)	0.3	1.96			
As	0.64(3)	0.12(8)	2.0(8)	4E-2	14.0			
Se	0.43(9)	0.22(13)	1.1(13)	6E-3	10.9			
Br	13.5(7)	5.8(6)	2.46(6)	3E-2	19.3			
Rb	12.9(7)	1.8(9)	24.8(8)	0.5	14.8			
Sr	33.0(4)	23.8(17)	3.9(22)	. 0.8	4.1			
Zr	11.0(11)	13.0(15)	< 0.7	0.7	282			
Мо	< 1.4	< 0.3	7.3(27)	1.41	53.1			
Ru	0.16(25)	< 0.1	< 0.01	0.01	3.63			
Ag	0.05(8)	0.02(7)	0.27(12)	3E-3	17.7			
Cd	< 0.1	< 0.1	0.15(27)	2E-3	48.0			
Sn	2.4(15)	1.7(10)	5.7(18)	2E-3	49.1			
Sb	0.37(6)	0.02(7)	0.36(9)	6E-4	28.8			
Te	< 0.1	< 0.1	0.11(37)	0.1	1.7			

Element	Element concentrations, pm							
	Moss DK-1	Lichen Usnea sp	Pine needles	Concentr. limit	$\frac{I_0}{\sigma_0}$			
I	3.8(8)	3.0(4)	< 1.0	0.11	24.8			
Cs	0.29(7)	0.016(9)	0.046(8)	3E-3	18.5			
Ba	18.5(8)	2.5(12)	2.0(46)	0.3	23.5			
Hf	0.21(14)	0.12	< 0.002	2E-3	2.52			
Ta	0.026(14)	0.016(13)	0.00057(20)	2E-4	33.3			
w	0.73(27)	< 0.2	0.34(12)	6E-2 <sup>1</sup>	13.7			
Re	< 0.001	< 0.001	< 0.0022(23)	1.0E-3	15.3			
Ir	< 0.0003	< 0.0002	0.0007(20)	5E-4	5.8			
Au	0.00074(20)	0.0008(8)	0.0073(7)	5E-5	15.7			
Hg	0.67(10)	< 0.05	< 0.02	2E-2	0.88			
Th	0.2(5)	< 0.02	0.0021(9)	1.0E-3	12.0			
U	0.19(5)	< 0.02	< 0.015	2.0E-2	102.3			

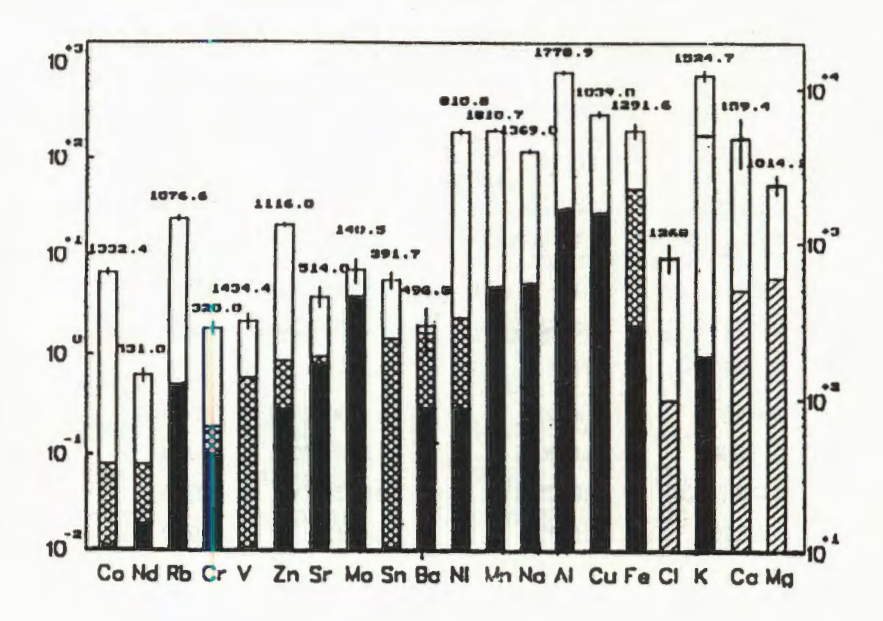
<sup>1 -</sup> detectrion limit for channel Ch.1.

Table 3. Concentration of REE in moss samples Hylocomium splendens, the lichen ones Usnea sp, pine needles Pinus sylvestris L, and the detection limits for pine needles in channel 3

Element		$I_0$			
	Moss DK-1	Lichen	Pine needles	Detect. limit	$\frac{I_0}{\sigma_0}$
La	1.22(7)	1.07(9)	0.13(13)	3.0E-3	1.24
Ce	2.92(8)	2.38(10)	0.16(19)	5.0E-2	0.82
Nd	0.92(26)	2.55(16)	0.56(15)	2.0E-2*	2.35
Sm	0.23(8)	0.46(6)	0.013(8)	1.4E-4 <sup>1</sup>	14.4
Eu	0.042(24)	0.060(11)	0.001(29)	5.0E-4 <sup>1</sup>	0.67/5.67**
Gd	0.21(14)	< 0.1	0.026(16)	1.0E-2	2.75
Tb	0.022(9)	0.089(8)	0.002(20)	5.0E-4	17.2
Tm	0.015(13)	0.14(6)	0.0019(30)	1.4E-3*	17.9
Yb	0.054(40)	0.012(10)	0.0065(28)	4.0E-3	0.44
Lu	0.028(29)	0.096(8)	< 0.002	2.0E-3	2.26

<sup>\*</sup>without Gd coat \*\* for <sup>152</sup>Eu

<sup>1 -</sup> detection limit for channel Ch.1.



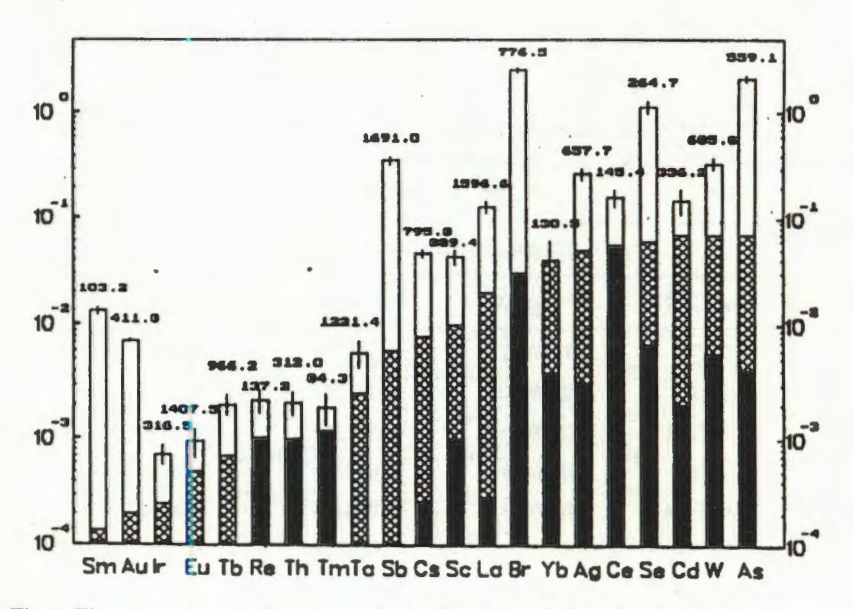


Fig. 1. Element concentrations (undashed columns) and detection limits for pine needles (Pechenga-Nickel) irradiated in Ch.1 (light-dashed columns) and Ch.3 (dark-dashed columns)

But at the same time, the Compton gamma quanta registered (especially in the case of Sc, Co and Fe) strongly «shadow» the peaks of other elements, thus lowering the detection limits.

Fast neutrons were used to determine concentrations of Ni from the  $^{58}$ Ni (n, p)  $^{58}$ Co reaction. It works well for INAA. But, on the other hand, density of fast neutrons on both channels of the IBR-2 reactor leads to the interference effect when the concentration of Al, Na, Mn, and Cr, is affected by the  $^{31}$ P  $(n, \alpha)$   $^{28}$ Al,  $^{28}$ Si (n, p)  $^{28}$ Al,  $^{27}$ Al  $(n, \alpha)$   $^{24}$ Na,  $^{54}$ Fe  $(n, \alpha)$   $^{51}$ Cr and reactions  $^{56}$ Fe (n, p)  $^{56}$ Mn, respectively.

Aluminium determination from the  $^{27}$ Al  $(n, \gamma)$   $^{28}$ Al reaction is essentially influenced by the interfering reaction in moss. Up to 50—60% of  $^{27}$ Al  $(n, \gamma)$   $^{28}$ Al is produced by  $^{31}$ P and  $^{28}$ Si. Thus, the real concentrations of Al given in Table 2 have a higher percentage of errors, because the concentration of P was not determined. In all other cases mentioned above, contribution of interfering reactions is insignificant: for Na it is 1%; for Mn, 0,1%; and 0.5% for Cr.

Data on confidence intervals for trace elements and REE are given in Tables 4 and 5. Element concentrations with their confidence intervals in moss and pine needles normalized to DK-1 values are shown in Fig.2. Data on lichens are listed in Table 3.

Table 4. Elements concentrations and confidence interval,  $\mu$ 

Element	Tver region (Dubna)				Kola Peninsula	
	Moss, ppm	μ, %	Pine needles, ppm	μ, %	Pine needles, ppm	μ,
Na	1190	36	56	53		
Mg	1780	31	1370	25		
Al	517	35	193	24		
Cl	1050	23	376	18		
K	9160	18	4300	18		
Ca	7800	40	6050	16	3180	25
Sc	0.066	60	0.018	68	0.11	30
V	1.52	55				
Cr	1.26	26			0.46	28
Mn	290	43	340	44		
Fe	306	39	57	76	132	25
Co	0.46	33	0.17	47	0.73	19
Ni	1.6	26	2.0	60	85	34
Cu	12.4	30	6.3	35		
Zn	39.3	31	35	34	31.6	27
As	0.25	73	3.1	35	0.72	52
Se	0.14	40	3.9	57	0.083	24
Br	3.1	30	1.8	42	4.7	21
Rb	66.1	32	24.7	48	33	16
Sr	27.0	30	11.4	40	11.7	64

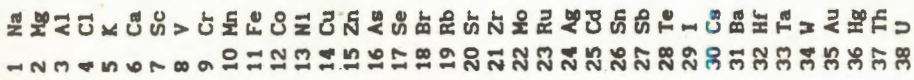
Element		Tver	Kola Peninsula			
	Moss, ppm	μ, %	Pine needles, ppm	μ, %	Pine needles, ppm	μ,
Zr	5.3					
Mo	0.44	57			1.14	42
Ag	3.5E-2	20	1.9E-2	34	0.0072	19
Cd	0.28	115			0.067	21
Sn	- 1				2.37	19
Sb	0.16	28	0.04	60	0.047	26
I	1.50	41				
Cs	0.22	37	4.4E-2	53	0.22	55
Ba	15.3	38	0.54	61	1.8	31
Hf	9.0	53	0.23	92	0.034	90
Ta	6.3E-3	54	1.2E-3	71	5.3E-4	49
w	1.9	44	0.96	80	0.46	50
Au	10.2E-3	70	1.9E-3	47	1.2E-3	8
Th	7.9E-2	66	9.4E-3	21	8.1E-3	11
U	0.052	85	,	ā	6.8E-3	54

 $<sup>\</sup>mu = \frac{SD}{n^{0.5}}t$ , t — student's factor for significance level 0.05,

Table 5. Concentrations of REE (ppm) and confidence interval,  $\mu$ 

Element		Tver	Kola Peninsula			
	Moss, ppm	μ, %	Pine needles	μ, %	Pine needles	μ, %
La	0.41	55	0.031	58	0.023	30
Се	1.00	100	1.02	100	0.21	11
Nd	_	-	_	_	0.6	17
Sm	0.042	52	0.0048	32	0.0104	14
Eu	0.0036	51	0.024	48	0.007	53
Gd	0.11	100	1.3	66	0.13	15
Tb	0.015	27	_	_	0.0029	41
Tm	0.028	28	_	_	0.011	34
Yb	0.024	50	0.013	64	0.0043	47
Lu	_	_	_		0.00046	41

SD — standard deviation, n — number of samples



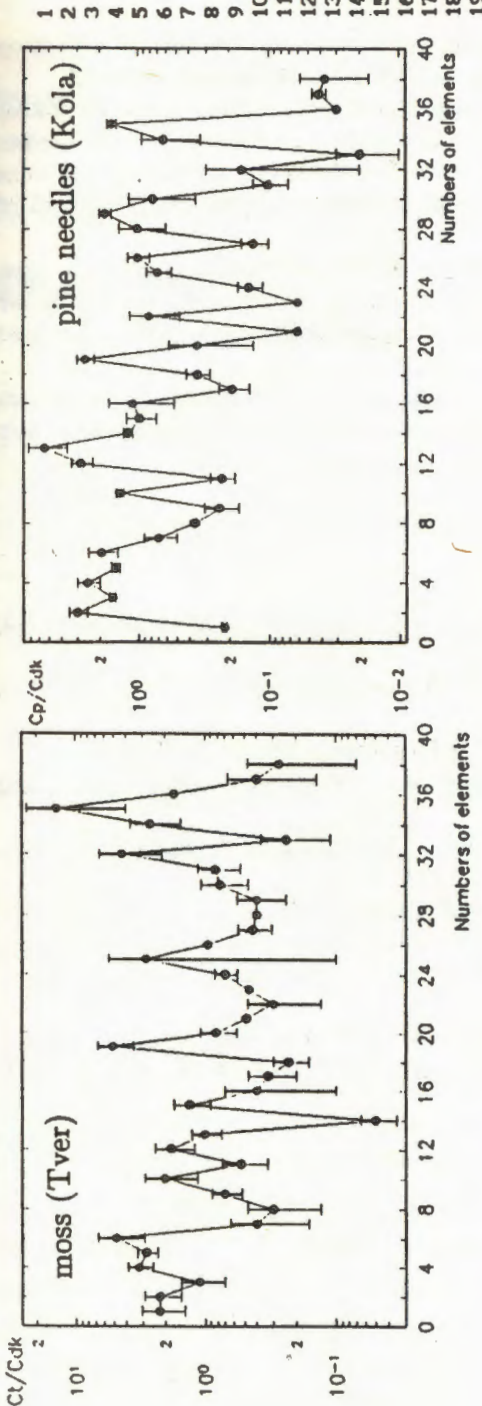
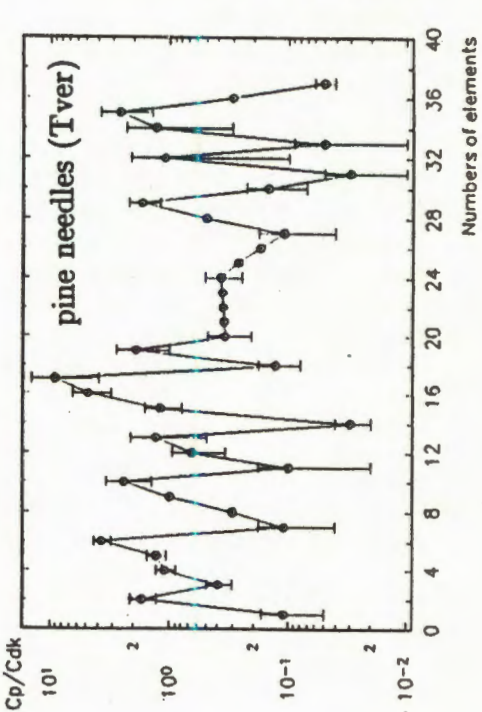


Fig.2. Element concentrations with their confidence intervals in moss and pine needles normalized to DK-1 values.  $C_m$  is a concentration in moss;  $C_p$  is a concentration in pine needles;  $C_{DK-1}$  is a concentration in DK-1 reference moss. Data for moss and pine needles (Tver) are obtained for 11 points along the perimeter of an area of 3000 sq. km. Data for pine needles (North-Nickel, Kola) are obtained for 7 trees.



#### Conclusion

Potentialities of the use of resonance neutrons for monitoring atmospheric deposition of heavy metals, including REE and a set of nonmetallic elements are demonstrated.

Data obtained for pine needles from Tver region and the Kola Peninsula are similar within the confidence intervals and are not very large. Confidence intervals for pine needles from the Kola Peninsula are lower, but samples from Tver region in the vicinity of Dubna were collected from the significantly smaller squares, along the perimeter of an area of 3000 sq.km.

Concentration values for pine needles for many elements are lower than those for moss samples. Concentrations of REE and some other elements in investigated pine needles are lower than those in DK-1. That is why to determine these concentrations we also used Gd-coated channel Ch.3.

In conclusion, authors express their deep gratitude to Prof. E.Steinnes for providing us with the reference material DK-1 for our investigations, and to Mrs. L.P.Strelkova for help in the preparation of this manuscript.

#### References

- Schaug J., Rambaek J.P., Steinnes E., Henry R.C. Atmospheric Environment, 1990, vol.24A, No.10, p.2625-2631.
- Steinnes E. In: Activation Analysis in Environment Protection. JINR D14-93-325, Dubna, 1993, p.59.
- 3. Steinnes E., Rambaek J., Hanssen J.E. Chemosphere, 1992, 25, p.735-752.
- 4. Steinnes E., Johansen O., Royset O., Degard M. Environmental Monitoring and Assessment, 1993, 25, p.87-97.
- Vostokova T.A., Ilyna Ye.A., Nazarov V.M. In: Activation Analysis in Environment Protection. JINR D14-93-325, Dubna, 1993.
- 6. Nazarov V.M. et al. J.Radioanal. and Nucl. Chem., 1993, vol.167, No.1, p.11-21.
- Frontasyeva M.V., Nazarov V.M., Steinnes E. In: «Heavy Metals in the Environment», vol.2, p.17, September 1993. Toronto, Canada; J.Radioanal. and Nucl. Chem., 1994, vol.181, No.2, p.363-371.
- Ostrovnaya T.M., Hefedyeva L.S., Nazarov V.M., Borzakov S.B., Strelkova L.P.
   — In: Activation Analysis in Environment Protection. JINR D14-93-325, Dubna, 1993, p.319.

УДК 539.123

#### TO THE THEORY OF NEUTRINO OSCILLATION

#### Kh.M. Beshtoev

The example of  $K^0$ -,  $\overline{K}^0$ -meson oscillations is utilized in showing that  $v_e$ ,  $v_\mu$ ,  $v_\tau$  oscillations must proceed via two stages. First  $v_e$ ,  $v_\mu$ ,  $v_\tau$ -eigenstates of the weak interactions are created. Then, owing to the presence of lepton number violating interactions, these neutrino states are converted into superpositions of  $v_1$ ,  $v_2$ ,  $v_3$ -eigenstates of interactions violating the lepton numbers. Further, neutrino oscillations will occur in accordance with the standard scheme.

The investigation has been performed at the Laboratory of Particle Physics, JINR.

#### К теории осцилляции нейтрино

#### Х.М.Бештоев

На примере  $K^0$ -,  $\overline{K}^0$ -осцилляций показано, что  $\nu_e$ -,  $\nu_\mu$ -,  $\nu_\tau$ -осциляции идут через две стадии. Сперва рождаются  $\nu_e$ -,  $\nu_\mu$ -,  $\nu_\tau$ -нейтрино — собственные состояния слабого взаимодействия. Затем, если присутствует взаимодействие, нарушающее лептонные числа, эти нейтринные состояния превращаются в суперпозиции  $\nu_1$ -,  $\nu_2$ -,  $\nu_3$ -нейтрино — собственные состояния взаимодействия, нарушающего лептонные числа. Далее осцилляция нейтрино будет происходить согласно стандартной схеме.

Работа выполнена в Лаборатории сверхвысоких энергий ОИЯИ.

#### 1. Introduction

In the old theory of neutrino oscillations [1], constructed by analogy with the theory of  $K^0$ ,  $\overline{K}^0$  oscillation, it is supposed that mass eigenstates are  $v_1$ ,  $v_2$ ,  $v_3$  neutrino states, but not physical neutrino states  $v_e$ ,  $v_\mu$ ,  $v_\tau$  and that the neutrinos  $v_e$ ,  $v_\mu$ ,  $v_\tau$  are created as superpositions of  $v_1$ ,  $v_2$ ,  $v_3$  states. This means that the  $v_e$ ,  $v_\mu$ ,  $v_\tau$  neutrinos have no definite mass, i.e., their masses may vary depending on the  $v_1$ ,  $v_2$ ,  $v_3$  admixture in the  $v_e$ ,  $v_\mu$ ,  $v_\tau$  states (naturally, in this case the momentum of the neutrinos is not conserved) Probably, this picture is incorrect one. This can be illustrated taking advantage of the  $K^0$ ,  $\overline{K}^0$  oscillations which have been well studied.

# 2. $K^0$ , $\overline{K}^0$ Oscillations

- 1) The  $K^0$ ,  $\overline{K}^0$  mesons, which consist of the s,  $\overline{s}$ , d,  $\overline{d}$  quarks, are created in the strong interactions (the typical times of strong interactions are  $t_{\rm str} \cong 10^{-23}$  s.) and are, accordingly, eigenstates of these interactions, i.e., the mass matrix of the  $K^0$ ,  $\overline{K}^0$  mesons is diagonal.
- 2) If we take into account the weak interaction (typical times of weak interactions are  $t_{\text{weak}} \cong 10^{-8} \text{ s.}$ ) which violates strangeness, then the mass matrix of  $K^0$ -mesons will become nondiagonal. If we diagonalize this matrix, then we will come to the  $K_1^0$ ,  $K_2^0$  states, which are eigenstates of the weak interaction [2].

So we can see that, if  $K^0$  mesons are created in strong interactions, then  $K^0$ ,  $\overline{K}^0$  mesons are produced, and if  $K^0$  mesons are created in weak interactions then  $K_1^0$ ,  $K_2^0$  mesons are created. In these cases no oscillations of  $K^0$  mesons will occur.

3) Now let us give a phenomenological description of  $K^0$ ,  $\overline{K}^0$  meson creation and oscillation processes. We will consider the creation of  $K^0$ ,  $\overline{K}^0$  mesons as a quasistationary process with a typical time  $t_{\rm str}$ . Within this typical time,  $-t_{\rm str}$ , weak interactions will violate strangeness and result in the mass matrix of the  $K^0$  mesons becoming nondiagonal. The probability for this process to occur in  $t = \pi t_{\rm str}$  is:

$$W(t = \pi t_{\text{str}}) = \frac{\left(1 - \exp\left(-\frac{t}{t_{\text{weak}}}\right)\right)}{\left(1 - \exp\left(-\frac{t}{t_{\text{str}}}\right)\right)} \cong$$

$$\stackrel{:}{\cong} \pi \frac{t_{\text{str}}}{t_{\text{weak}}} \cong \pi \ 10^{-15},$$
(1)

where  $\left(1 - \exp\left(-\frac{t}{t_{\text{str, weak}}}\right)\right)$  — is the decay probability of the quasistationary state during the time — t.

The mass matrix of the  $K^0$  mesons will become nondiagonal in  $t = \pi \cdot 10^{-23}$  s with a probability of  $W \cong \pi \cdot 10^{-15}$ . And then the  $K_1^0$ ,  $K_2^0$  mesons — eigenstates of weak interactions will be created. So we can see that in this case mainly  $K^0$ ,  $\overline{K}^0$  mesons will be produced, but not the  $K_1^0$ ,  $K_2^0$  mesons.

Then, when the  $K^0$ ,  $\overline{K}^0$  mesons, that were created in strong interactions, pass through vacuum, the mass matrix of the  $K^0$  mesons will become nondiagonal, owing to the presence of weak interactions violating strangeness. Diagonalizing it, we get  $K_1^0$ ,  $K_2^0$ -meson states which are eigenstates of weak interactions. Obviously, the  $K^0$ ,  $\overline{K}^0$  mesons are, then, converted into superpositions of  $K_1^0$ ,  $K_2^0$  mesons [2].

$$K^{0} = \frac{K_{1}^{0} + K_{2}^{0}}{\sqrt{2}}, \quad \overline{K}^{0} = \frac{K_{1}^{0} - K_{2}^{0}}{\sqrt{2}}.$$
 (2)

Then, oscillations of the  $K^0$ ,  $\overline{K}^0$  mesons will take place on a background of  $K_1^0$ ,  $K_2^0$  decays. The length of these oscillations is [3]:

$$L_{\rm osc}(m) = \frac{2.48 p_K^0 \,(\text{MeV})}{|m_{K_1^0 K_1^0} - m_{K_2^0 K_2^0}|^2 \,(\text{eV})^2},$$
(3)

 $p_{\kappa^0}$  is the momentum of  $K^0$ .

The main question which arises now is: which type of oscillations — real (implying actual transitions between the particle) or virtual (implying virtual transitions between particle without transition to mass shells) takes place between the  $K^0$ ,  $\overline{K}^0$  mesons? Since the masses of  $K^0$  and  $\overline{K}^0$  mesons are equal, oscillations between these mesons are real. But, if the masses of  $K^0$  and  $\overline{K}^0$  mesons were not equal, then the oscillations would be virtual [4].

### 3. v-Oscillations

We can now pass to the analysis of neutrino oscillations, taking advantage of the example of  $K^0$ ,  $\overline{K}^0$ -meson oscillations.

- 1) The physical states of the  $v_e$ ,  $v_\mu$ ,  $v_\tau$  neutrinos are eigenstates of the weak interaction and, naturally, the mass matrix of  $v_e$ ,  $v_\mu$ ,  $v_\tau$  neutrinos is diagonal. All the available experimental results indicate that the lepton numbers  $l_e$ ,  $l_\mu$ ,  $l_\tau$  are well conserved, i.e., the standard weak interactions do not violate the lepton numbers.
- 2) Then, to violate the lepton numbers, it is necessary to introduce an interaction violating these numbers. It is equivalent to indroducing nondiagonal mass terms in the mass matrix of  $v_e$ ,  $v_\mu$ ,  $v_\tau$ . Diagonalizing this matrix we go to the  $v_1$ ,  $v_2$ ,  $v_3$  neutrino states. Exactly like the case of  $K^0$  mesons creating in strong interactions, when mainly  $K^0$ ,  $\overline{K}^0$  mesons are produced, in the considered case  $v_e$ ,  $v_\mu$ ,  $v_\tau$ , but not  $v_1$ ,  $v_2$ ,  $v_3$ , neutrino states are mainly created in the weak interactions (this is so, because the contribution of the lepton numbers violating interactions in this process is too small).
- 3) Then, when the  $v_e$ ,  $v_\mu$ ,  $v_\tau$  neutrinos pass through vacuum, they will be converted into superpositions of the  $v_1$ ,  $v_2$ ,  $v_3$  owing to presence of the interactions violating the lepton numbers of neutrinos and will be left on their mass shells. And, then, oscillations of the  $v_e$ ,  $v_\mu$ ,  $v_\tau$  neutrinos will take place according to the standard scheme [1]. Whether these oscillations are real or virtual will be determined by the masses of the physical neutrinos

 $v_e$ ,  $v_\mu$ ,  $v_\tau$ . i) If the masses of the  $v_e$ ,  $v_\mu$ ,  $v_\tau$  neutrinos are equal, then real oscillation of the neutrinos will take place. ii) If the masses of the  $v_e$ ,  $v_\mu$ ,  $v_\tau$  are not equal, then virtual oscillation of the neutrinos will take place. To make these oscillations real, these neutrinos must participate in the quasielastic interactions, in order to undergo transition to the mass shell of the other appropriate neutrinos by analogue with  $\gamma - \rho^0$  transition in the vector meson dominance model. In case ii), enhancement of neutrino oscillations will take place if the neutrinos pass through a bulk of matter [5].

### References

- Boehm F., Vogel P. Cambridge Univ. Press, 1987, p.27, p.121.
   Bilenky S.M., Petrov S.T. Rev. of Mod. Phys., 1987, 59, p.631.
- Beshtoev Kh.M. Turk. Journ. of Phys., 1994, 18, p.787.
- 3. Okun L.B. Leptons and Quarks, M., 1990.
- 4. Beshtoev Kh. M. JINR, E2-92-318, Dubna, 1992.
- 5. Beshtoev Kh.M. JINR, E2-94-46, Dubna, 1994.

УДК 539.142.3+539.143.44

# COUPLED QUADRUPOLE AND MONOPOLE VIBRATIONS OF LARGE AMPLITUDE

# E.B.Balbutsev, I.V.Molodtsova, P.Schuck\*

The set of nonlinear dynamical equations for quadrupole and monopole moments of nuclei is derived from the equation for Wigner function  $f(\mathbf{r}, \mathbf{p}, t)$  with the help of the method of Wigner function moments. These equations are solved numerically for <sup>208</sup>Pb. The giant quadrupole and monopole resonances are reproduced very well. The corresponding multiphonon states are predicted.

The investigation has been performed at the Bogoliubov-Laboratory of Theoretical Physics, JINR.

# Связанные квадрупольные и монопольные колебания большой амплитуды

# Е.Б.Бальбуцев, И.В.Молодцова, П.Шук

Из уравнения для функции Вигнера  $f(\mathbf{r}, \mathbf{p}, t)$  с помощью метода моментов функции Вигнера выведена система нелинейных динамических уравнений для квадрупольного и монопольного моментов ядра. Полученные уравнения решены численно для  $^{208}$ Pb. Хорошо воспроизводятся энергии гигантских квадрупольного и монопольного резонансов. Предсказаны соответствующие мультифононные резонансы.

Работа выполнена в Лаборатории теоретической физики им. Н.Н.Боголюбова ОИЯИ.

### 1. Introduction

Large amplitude motion is very interesting and complicated field of nuclear physics. There are not so much methods and models treating this problem ([1], [2], [3] and references therein), so every new result here is valuable.

In this paper we use the method of Wigner function moments in the frame of TDHF theory with the simple Hamiltonian to derive the set of nonlinear dynamical equations for the quadrupole and monopole moments of nucleus. This model is attractive, because it allows one to write exact equations, which can be solved exactly. And what is more, it can be generalized to become rather realistic.

<sup>\*</sup>ISN, Grenoble, France

# 2. Equations of motion

2.1. Description of the Model. Our model is based on the equation for a one-body density matrix  $\hat{\rho} = \rho(\mathbf{r}_1, \mathbf{r}_2, t)$  in the TDHF theory:

$$\frac{\partial \hat{\rho}}{\partial t} = [\hat{H}, \, \hat{\rho}] \,. \tag{1}$$

We transform it into the equation for Wigner function [4]

$$f(\mathbf{r}, \mathbf{p}, t) = \frac{1}{(2\pi h)^3} \int e^{-i\mathbf{p}\cdot\mathbf{n}'} h \rho(\mathbf{r} + \frac{\mathbf{s}}{2}, \mathbf{r} - \frac{\mathbf{s}}{2}, t) d\mathbf{s}:$$

$$\frac{\partial f}{\partial t} = \frac{2}{h} \sin\left\{\frac{h}{2} (\nabla_{\mathbf{r}}^H \cdot \nabla_{\mathbf{p}}^f - \nabla_{\mathbf{p}}^H \cdot \nabla_{\mathbf{r}}^f)\right\} H_W f, \qquad (2)$$

where upper index of nabla shows the function which this operator acts on,  $H_W$  is the Wigner transform of the Hamiltonian:

$$H_{\mathbf{W}}(\mathbf{r}, \mathbf{p}) = \int e^{-i\mathbf{p}\cdot\mathbf{s}/h} (\mathbf{r} + \frac{\mathbf{s}}{2}|H|\mathbf{r} - \frac{\mathbf{s}}{2}) d\mathbf{s}$$
.

If the Hamiltonian is the sum of the kinetic energy and the local potential  $V(\mathbf{r})$ , its Wigner transform is just the classical version of the same Hamiltonian:  $H_W = \frac{p^2}{2m} + V(\mathbf{r})$ . Then equation (2) becomes:

$$\frac{\partial f}{\partial t} + \frac{1}{m} \mathbf{p} \cdot \nabla_{\mathbf{p}} f = \frac{2}{h} \sin \left( \frac{h}{2} \nabla_{\mathbf{r}}^{V} \cdot \nabla_{\mathbf{p}}^{f} \right) V f.$$
 (3)

Our model potential is the harmonic oscillator with the quadrupole-quadrupole residual interaction:  $V(\mathbf{r}, t) = \frac{1}{2}m\omega^2r^2 + \lambda q(t)Q(\mathbf{r})$ , where  $Q(\mathbf{r}) = x_1^2 + x_2^2 - 2x_3^2$ ,  $q(t) = trQ\rho = \int d\mathbf{r}d\mathbf{p}Q(\mathbf{r})f(\mathbf{r}, \mathbf{p}, t)$ . Only the first term of the sin-operator survives in this case and we have:

$$\frac{\partial f}{\partial t} + \frac{1}{m} \sum_{i=1}^{3} p_i \frac{\partial f}{\partial x_i} - \sum_{i=1}^{3} \frac{\partial V}{\partial x_i} \frac{\partial f}{\partial p_i} = 0 , \qquad (4)$$

with

$$\frac{\partial V}{\partial x_i} = [m\omega^2 + 2\lambda q(t)(\delta_{i1} + \delta_{i2} - 2\delta_{i3})]x_i.$$
 (5)

2.2. Wigner Function Moments. Now we apply the method of Wigner function moments [5] to derive the closed system of the dynamical equations for cartesian tensors of a second rank. Integrating equation (4) over the phase space  $\{\mathbf{r},\mathbf{p}\}$  with the weights  $\mathbf{x}_{x_j}$ ,  $p_i x_j$ ,  $p_j x_j$ , we get:

$$\int x_i x_j \frac{\partial n(\mathbf{r}, t)}{\partial t} d\mathbf{r} + \int x_i x_j \frac{\partial (n(\mathbf{r}, t) u_s(\mathbf{r}, t))}{\partial x_s} d\mathbf{r} = 0,$$
 (6)

$$m \int x_j \frac{\partial}{\partial t} \left( n(\mathbf{r}, t) u_i(\mathbf{r}, t) \right) d\mathbf{r} + \int n(\mathbf{r}, t) x_j \frac{\partial V}{\partial x_i} d\mathbf{r} + \frac{1}{m} \int x_j \frac{\partial}{\partial x_s} \mathcal{A}_{si} \left( \mathbf{r}, t \right) d\mathbf{r} = 0 , \qquad (7)$$

$$\frac{\partial}{\partial t} \int \mathcal{A}_{ij}(\mathbf{r}, t) d\mathbf{r} + m \int n(\mathbf{r}, t) \left[ u_i(\mathbf{r}, t) \frac{\partial V}{\partial x_j} \right]_{ij} d\mathbf{r} + \frac{1}{m} \int \frac{\partial}{\partial x_s} \mathcal{A}_{sij}(\mathbf{r}, t) d\mathbf{r} = 0 , \qquad (8)$$

where  $[...]_{ij}$  means that the quantity into brackets is symmetrized with respect to idexes i and  $j([a_ib_j]_{ij} = a_ib_j + a_jb_i)$  and the summation over repeated indexes is assumed. Here we have introduced the notations:  $n(\mathbf{r}, t) = \int f(\mathbf{r}, \mathbf{p}, t)d\mathbf{p}$ ,  $mn(\mathbf{r}, t)u_i(\mathbf{r}, t) = \int p_if(\mathbf{r}, \mathbf{p}, t)d\mathbf{p}$ ,  $A_{ij...k}(\mathbf{r}, t) = \int p_ip_j...p_kf(\mathbf{r}, \mathbf{p}, t)d\mathbf{p}$ . By definition  $n(\mathbf{r}, t)$  is the nucleon density,  $\mathbf{u}(\mathbf{r}, t)$  is the mean velocity of nucleons,  $A_{ij}(\mathbf{r}, t)/2m$  is the kinetic energy tensor (or pressure tensor). Integrating by parts the last terms in (6)—(8) and introducing the notations  $J_{ij}(t) = \int x_i x_j n(\mathbf{r}, t) d\mathbf{r}$  for an inertia tensor and  $\Pi_{ij}(t) = \int A_{ij}(\mathbf{r}, t) d\mathbf{r}$  for an integral kinetic energy tensor we have:

$$\frac{d}{dt}J_{ij}(t) - \left[\int x_j n(\mathbf{r}, t) u_i(\mathbf{r}, t) d\mathbf{r}\right]_{ij} = 0, \qquad (9)$$

$$m\frac{d}{dt}\int x_j n(\mathbf{r}, t)u_i(\mathbf{r}, t)d\mathbf{r} + \int x_j n(\mathbf{r}, t)\frac{\partial V}{\partial x_i}d\mathbf{r} - \frac{1}{m}\Pi_{ij}(t) = 0,$$
 (10)

$$\frac{d}{dt} \Pi_{ij}(t) + m \int n(\mathbf{r}, t) \left[ u_i(\mathbf{r}, t) \frac{\partial V}{\partial x_i} \right]_{ij} d\mathbf{r} = 0.$$
 (11)

The last integral of the equation (8) with the third rank tensor  $A_{sij}$  has disappeared due to the evident boundary condition  $A_{sij}(\mathbf{r}, t) \to 0$  at  $\mathbf{r} \to \infty$ , which follows from the boundary condition for the Wigner function  $f(\mathbf{r}, \mathbf{p}, t) \to 0$  at  $\mathbf{r} \to \infty$ . As a result we are left with the closed system of equations for second rank tensors.

The equations (9) and (11) are evidently symmetrical with respect to indexes i, j and the equation (10) has not the definite symmetry. We can construct easily the symmetrical and antisymmetrical equations by combinations of the equation (10) with different indexes:

$$m \frac{d}{dt} \left[ \int x_j n(\mathbf{r}, t) u_i(\mathbf{r}, t) d\mathbf{r} \right]_{ij} + \left[ \int x_j n(\mathbf{r}, t) \frac{\partial V}{\partial x_i} d\mathbf{r} \right]_{ij} - \frac{2}{m} \Pi_{ij}(t) = 0, \tag{12}$$

$$m \frac{d}{dt} \int n(\mathbf{r}, t) \{x_j u_i(\mathbf{r}, t) - x_i u_j(\mathbf{r}, t)\} d\mathbf{r} = -\int n(\mathbf{r}, t) \{x_j \frac{\partial V}{\partial x_i} - x_i \frac{\partial V}{\partial x_j}\} d\mathbf{r}.$$
 (13)

The integral on the left-hand side of the equation (13) is the angular momentum of the nucleus. When  $V(\mathbf{r}, t)$  is a self-consistent potential, the right-hand side of this equation is equal to zero and the equation expresses the angular momentum conservation law. For our model potential

$$x_j \frac{\partial V}{\partial x_i} - x_i \frac{\partial V}{\partial x_j} = 2\lambda q(t)x_j x_i (\delta_{i1} - \delta_{j1} + \delta_{i2} - \delta_{j2} - 2\delta_{i3} + 2\delta_{j3}).$$

This expression is different from zero for j=3, i=1, 2 or i=3, j=1, 2 and proportional to  $x_1x_3$  or  $x_2x_3$ . The corresponding integral  $\int n(\mathbf{r}, t)x_1x_3d\mathbf{r}$  is equal to zero, because our potential does not destroy the triplanar symmetry of the nucleon distribution  $n(\mathbf{r}, t)$ . Therefore our model conserves the angular momentum.

The non-trivial information is contained in the symmetrical equation (12). We transform it using the equation (9) and the expression (5) for the potential derivative:

$$m\frac{d^2}{dt^2}J_{ij}(t) + 2J_{ij}(t) \left\{m\omega^2 + \lambda q(t) \left(\delta_{i1} + \delta_{j1} + \delta_{i2} + \delta_{j2} - 2\delta_{i3} - 2\delta_{j3}\right)\right\} - \frac{2}{m}\Pi_{ij}(t) = 0. (14)$$

By definition  $q(t) = J_{11}(t) + J_{22}(t) - 2J_{33}(t)$ , hence this equation is nonlinear in  $J_{ij}$ . As is seen from its structure we can write the set of coupled dynamical equations for the tensors  $J_{11} + J_{22}$  and  $J_{33}$ :

$$m(\ddot{J}_{11} + \ddot{J}_{22}) + 2(J_{11} + J_{22}) \{m\omega^2 + 2\lambda(J_{11} + J_{22} - 2J_{33})\} - \frac{2}{m}(\Pi_{11} + \Pi_{22}) = 0,$$
 (15)

$$mJ_{33} + 2J_{33} \{m\omega^2 - 4\lambda (J_{11} + J_{22} - 2J_{33})\} - \frac{2}{m} \Pi_{33} = 0,$$
 (16)

where dot means the time derivative and we don't write out the time dependence of tensors for simplicity. To be closed, this system must be supplemented with the dynamical equations for the tensors  $\Pi_{11} + \Pi_{22}$  and  $\Pi_{33}$ . They are easily obtained from the equation (11):

$$\frac{d}{dt} \Pi_{ii}(t) + 2m\{m\omega^2 + 2\lambda q(t) (\delta_{i1} + \delta_{i2} - 2\delta_{i3})\} \int n(\mathbf{r}, t)u_i(\mathbf{r}, t)x_i d\mathbf{r} = 0.$$
 (17)

Using here equation (9) we have:

$$(\dot{\Pi}_{11} + \dot{\Pi}_{22}) + m(\dot{J}_{11} + \dot{J}_{22}) \{ m\omega^2 + 2\lambda(J_{11} + J_{22} - 2J_{33}) \} = 0, \tag{18}$$

$$\dot{\Pi}_{33} + m\dot{J}_{33} \{m\omega^2 - 4\lambda(J_{11} + J_{22} - 2J_{33})\} = 0.$$
 (19)

As one sees from the structure of the equations (15)-(19), it will be more convenient to rewrite them in terms of new variables: the component of the quadrupole moment

 $Q_{20} = J_{11} + J_{22} - 2J_{33}$ , the mean square radius  $Q_{00} = J_{11} + J_{22} + J_{33}$  and the irreducible tensors  $\Pi_{20} = \Pi_{11} + \Pi_{22} - 2\Pi_{33}$  and  $\Pi_{00} = \sum_{s=1}^{3} \Pi_{ss}$ . Taking the simple combinations of the equations (15), (16) and (18), (19) we get finally:

$$\begin{split} m^2 \ddot{Q}_{00} + 2m^2 \omega^2 Q_{00} + 4m\lambda Q_{20}^2 - 2\Pi_{00} &= 0, \\ m^2 \ddot{Q}_{20} + 2m^2 \omega^2 Q_{20} + 4m\lambda Q_{20}(2Q_{00} - Q_{20}) - 2\Pi_{20} &= 0, \\ \dot{\Pi}_{00} + m^2 \omega^2 \dot{Q}_{00} + 2m\lambda Q_{20} \dot{Q}_{20} &= 0, \\ \dot{\Pi}_{20} + m^2 \omega^2 \dot{Q}_{20} + 2m\lambda Q_{20}(2\dot{Q}_{00} - \dot{Q}_{20}) &= 0. \end{split} \tag{20}$$

Third equation of this system gives the integral of motion:

$$\Pi_{00} + m^2 \omega^2 Q_{00} + m \lambda Q_{20}^2 = const. \tag{21}$$

# 3. Analysis of the Equations of Motion

3.1. Stationary Solution. Investigating the stationary solution of the system (20) we can do some conclusion about the equilibrium shape of nuclei. By definition the variables of the stationary solution (or equilibrium state) don't depend on the time. Supposing the time derivatives in (20) equal to zero one gets two relations

$$m^{2}\omega^{2}Q_{00} + 2m\lambda Q_{20}^{2} - \Pi_{00} = 0,$$
  

$$m^{2}\omega^{2}Q_{20} + 2m\lambda Q_{20}(2Q_{00} - Q_{20}) - \Pi_{20} = 0.$$
 (22)

We shall call them equations of equilibrium. The second relation is of a special importance — it says that it is impossible to have a static quadrupole deformation  $(Q_{20} \neq 0)$  without a Fermi surface deformation  $(\Pi_{20} \neq 0)$  and vice versa [6]. Formally one can find non-trivial solution for  $Q_{20}$  having  $\Pi_{20} = 0$ :

$$Q_{20} = 2Q_{00} + \frac{m\omega^2}{2\lambda} \,. \tag{23}$$

However it turns out, that for the self-consistent force constant [1, 7]

$$\lambda = \lambda_{\text{Bohr}} = \frac{-m\omega^2}{4A < r^2 >} \tag{24}$$

the expression (23) is equal to zero (we remind that  $Q_{00} = A < r^2$ ).

3.2. Small Amplitude Approximation. Let us consider the system (20) in the small amplitude approximation. Taking the variations  $Q_{\lambda 0}(t) = Q_{\lambda 0}(0) + \delta Q_{\lambda 0}(t)$ ,  $\Pi_{\lambda 0}(t) = \Pi_{\lambda 0}(0) + \delta \Pi_{\lambda 0}(t)$  and neglecting the terms quadratic in  $\delta$ , one obtains two independent systems: the system for quadrupole tensors,

$$m^{2}\delta\ddot{Q}_{20} + (2m^{2}\omega^{2} + 8m\lambda Q_{00}(0)) \delta Q_{20} - 2\delta\Pi_{20} = 0,$$
  
$$\delta\dot{\Pi}_{20} + m^{2}\omega^{2}\delta\dot{Q}_{20} = 0,$$
 (25)

and the system for monopole tensors,

$$m^{2}\delta\ddot{Q}_{00} + 2m^{2}\omega^{2}\delta Q_{00} - 2\delta\Pi_{00} = 0,$$
  
$$\delta\dot{\Pi}_{00} + m^{2}\omega^{2}\delta\dot{Q}_{00} = 0.$$
 (26)

We consider the spherical nuclei in this paper, so we put everywhere  $Q_{20}(0) = 0$ . Supposing the time dependence  $e^{i\Omega t}$  for all variables one can find easily the next eigenfrequencies:

$$\Omega_0 = 2\omega \tag{27}$$

for the monopole vibrations and

$$\Omega_2 = 2 \sqrt{\omega^2 + \frac{2\lambda}{m} Q_{00}(0)}$$
 (28)

for the quadrupole vibrations. Using in (28) the expression (24) for the force constant one obtains the well-known [1, 7] result for the quadrupole eigenfrequency

$$\Omega_{2} = \sqrt{2} \, \omega \,. \tag{29}$$

The energies  $E_0 = h\Omega_0$  and  $E_2 = h\Omega_2$  are in qualitative agreement with experimental values of the energies of the monopole and quadrupole giant resonances (for  $h\omega = 41A^{-1/3}$  MeV).

So, in the small amplitude approximation our model gives only two levels, which can be interpreted as giant 0<sup>+</sup> and 2<sup>+</sup> resonances. This is true also for the calculations with realistic interactions [8].

3.3. Numerical Solution and Fourier Analysis. Principally another situation is observed in general case, when the system (20) is solved without any approximations. We solve it numerically with the help of Runge-Kutta procedure. The solutions depend strongly on the initial conditions (i.c.).

They can be chosen in two ways. In the first case one takes the equilibrium values (i.e. satisfying eqs. (22)) for the moments  $Q_{\lambda 0}(0)$ ,  $\Pi_{\lambda 0}(0)$  and some definite (nonzero) values for their derivatives  $\dot{Q}_{\lambda 0}(0)$ ,  $\dot{\Pi}_{\lambda 0}(0)$ . From the physical point of view that means that one pushes the nucleus and forces it to deviate from the state of equilibrium. In another case one takes some nonequilibrium values for  $Q_{\lambda 0}(0)$ ,  $\Pi_{\lambda 0}(0)$  and zero values for their derivatives. In such a way one deviates the nucleus from the equilibrium «by hand» and it begins to vibrate due to the restoring force.

It is evident, that both variants are equivalent: for any set of the initial values of  $Q_{\lambda 0}(0)$ ,  $\Pi_{\lambda 0}(0)$ ,  $Q_{\lambda 0}(0)$ ,  $\Pi_{\lambda 0}(0)$  from the first variant one can always find the corresponding set in the second variant to get the equivalent final results.

In this paper the first variant is used. We take  $Q_{20}(0) = \Pi_{20}(0) = 0$  because we deal with spherical nuclei. The evident approximation is used for the monopole momentum:  $Q_{00}(0) = \frac{3}{5} R_0^2 A$ , where  $R_0 = 1.18 A^{1/3}$ . The initial value  $\Pi_{00}(0)$  is fixed by the first equation of the system (22). The initial values for the time derivatives  $Q_{00}(0)$  and  $Q_{20}(0)$  are arbitrary. We have performed the calculations for two values of the force constant  $\lambda$  and for six sets of  $Q_{00}(0)$ ,  $Q_{20}(0)$ : 1) 6100, 10000, 2) 5000, 15000, 3) 5000, 18000, 4) 6100, 10, 5) 10, 10000, 6) 10, 10 (all the values are in MeV · fm²). The time-dependence of the function  $Q_{20}(t)$  for the first variant of i.c. with  $\lambda = \lambda_{\text{Bohr}}$  is demonstrated by the figure. As one can see, it oscillates quite irregularly. The maximal period of oscillations, when the curve begins to repeat itself, is  $\tau_2 = 457.4 \text{ MeV}^{-1} \cdot (\tau = t/h)$ . The pictures for other functions and other variants of i.c. are more or less similar. Having the periods of oscillation one can perform the Fourier analysis of the curves and represent all the functions by series

$$f(t) = \frac{a_0}{2} + \sum_i (a_i \cos \omega_i t + b_i \sin \omega_i t).$$

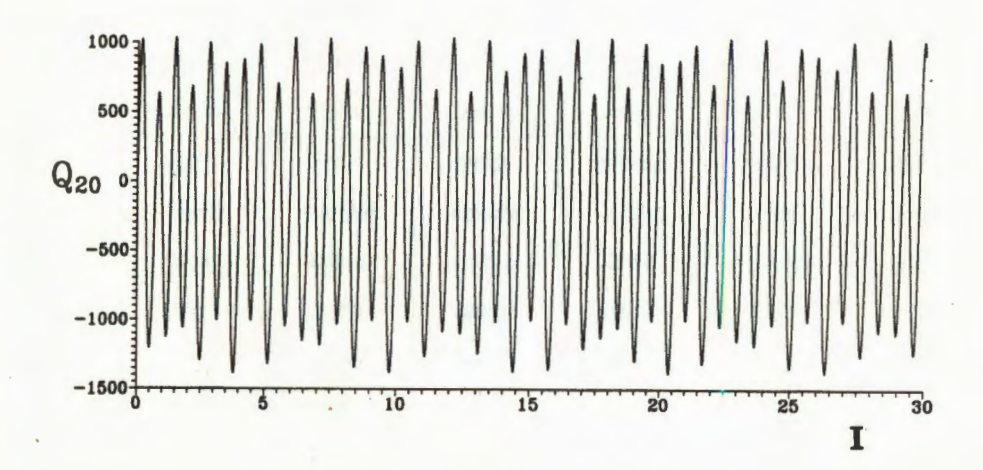


Fig. The time-dependence  $(\tau = t/h)$  of the quadrupole moment for  $\lambda = \lambda_{Bohr}$  and the initial conditions  $\dot{Q}_{00}(0) = 6100$ ,  $\dot{Q}_{20}(0) = 10^4$ 

Table 1. Fourier coefficients and energies for  $Q_{00}(0) = 6100$ ,  $Q_{20}(0) = 10^4$ 

i	hω, MeV		Q	00	Q	20
			b <sub>i</sub>	a <sub>i</sub>	bi	ai
0	0.00		0.000	69.547	0.000	-346.892
1	1.14	3Q-2M	-2.729	-0.735	9.464	2.550
2	1.90	5M-7Q	0.000	0.000	0.003	0.004
3	2.28	6Q-4M	0.006	-0.010	-0.038	0.065
4	3.04	3M-4Q	-0.086	0.035	0.407	-0.167
5	3.42	9Q-6M	0.000	0.000	-0.001	-0.002
6	4.18	M-Q	-0.641	-5.152	26.682	213.580
7	5.32	2Q-M	16.475	2.312	-46.538	-6.508
8	6.07	6M-8Q	0.000	0.000	0.001	0.001
9	6.46	5Q-3M	-0.005	0.012	0.015	-0.035
10	7.21	4M-5Q	0.029	-0.016	-0.172	0.097
11	8.35	2M-2Q	0.818	3.234	-8.459	-33.331
12	9.49	Q	-37.702	-0.585	1008.723	14.817
13	10.63-	4Q-2M-	0.342	-1.194	0.865	-3.034
14	11.39	5M-6Q	0.001	0.001	-0.029	0.021
15	11.77	7Q-4M	0.008	0.005	0.014	0.008
16	12.53	3M-3Q	-0.703	-1.803	-0.983	-2.512
17	13.67	М	461.418	-50.204	53.062	-5.838
18	14.81	3Q-M	2.606	-16.684	-0.640	4.139
19	15.95	6Q-3M	-0.020	-0.008	0.014	0.006
20	16.70	4M-4Q	-0.006	-0.011	0.029	0.053
21	17.84	2M-Q	1.833	-0.433	-7.259	1.729
22	18.98	2Q	-1.073	34.542	0.703	-23.925
23	20.12	5Q-2M	0.179	0.054	-0.128	-0.038
24	22.02	3M-2Q	0.238	-0.088	0.347	-0.130

i	hω <sub>i</sub> , MeV		Q	200	Q	20
			b <sub>i</sub>	a <sub>i</sub>	b <sub>i</sub>	a <sub>i</sub>
25	23.16	Q+M	0.199	2.142	1.069	11.233
26	24.30	4Q-M	-0.140	-0.024	0.628	0.107
27	25.44	7Q-3M	0.000	0.000	0.001	-0.002
28	26.20	4M-3Q	-0.005	0.002	0.029	-0.015
29	27.34	2M	-0.041	-0.187	0.145	0.651
30	28.48	3Q	0.453	0.021	-1.055	-0.046
31	29.62	6Q-2M	0.001	-0.004	-0.003	0.009
32	31.51	3M-Q	0.001	+0.002	-0.012	-0.035
33	32.65	2Q+M	-0.130	0.010	0.191	-0.015
34	33.79	5Q-M	-0.001	0.009	0.003	-0.017
35	36.83	2M+Q	-0.015	0.000	-0.025	0.005
36	37.97	4Q	0.001	0.000	-0.002	0.027
37	41.00	3M	0.001	0.000	-0.003	0.001

Table 2. Fourier coefficients and energies for  $\dot{Q}_{00}(0)=5000,~\dot{Q}_{20}(0)=15000$ 

i	hω <sub>i</sub> , MeV		Q	200	Q	$Q_{20}$
-			, b <sub>i</sub>	$a_i$	b <sub>i</sub>	$a_i$
0	0.000		0.000	159.3703	0.0000	-629.2916
1	0.632	7M-10Q	-0.0016	-0.0003	0.0095	0.0026
2	1.155	3Q-2M	-6.2262	-6.8901	26.2050	29.0060
3	1.787	5M-7Q	-0.0027	0.0012	0.1114	-0.0543
4	2.310	6Q-4M	0.0315	0.0031	-0.5563	-0.0557
5	2.942	3M-4Q	-0.1478	0.3773	-0.1133	0.2919
6	3.466	9Q-6M	0.0043	-0.0034	-0.0185	0.0163
7	4.097	M-Q	-4.8411	-12.7965	108.3201	286.6512
8	4.621	12Q-8M	-0.0003	0.0003	-0.0001	-0.0034

i	hω, , MeV	·	Q	200	Q	20
			bi	a <sub>i</sub>	b <sub>i</sub>	ai
9	5.253	2Q-M	32.5877	16.7307	-81.0800	-41.6762
10	5.884	6M-8Q	-0.0018	0.0025	-0.0098	0.0084
11	6.408	5Q-3M	0.3342	-0.0889	-1.0585	0.2804
12	7.040	4M-5Q	0.0040	-0.3266	-0.0159	1.2394
13	7.563	8Q-5M	-0.0116	0.0185	0.0522	-0.0833
14	8.195	2M-2Q	7.9911	9.0500	-56.5284	-64.1159
15	8.827	9M-12Q	0.0006	-0.0001	-0.0027	0.0020
16	9.350	Q	-96.8501	-10.9563	1496.3934	170.5650
17	9.982	7M-9Q	-0.0001	-0.0011	-0.0107	0.0273
18	10.505	4Q-2M	5.0277	-3.6061	18.3302	-13.1196
19	11.137	5M-6Q	-0.0197	-0.0539	0.0514	0.1395
20	11.660	7Q-4M	0.0037	-0.0177	-0.0295	0.1365
21	12.292	3M-3Q	-3.6049	-1.9033	-8.5572	-4.5308
22	12.815	10Q-6M	0.0111	0.0193	0.0057	0.0081
23	12.924	10M-13Q	-0.0004	0.0006	0.0008	0.0002
24	13.447	м .	399.0070	-101.4652	102.3071	-25.8836
25	13.970	13Q-8M	0.0020	0.0014	-0.0008	0.0001
26	14.079	8M-10Q	-0.0006	-0.0044	-0.0005	0.0005
27	14.602	3Q-M	31.9651	-48.0564	-5.7075	8.5558
28	15.234	6M-7Q	0.0095	0.0097	0.0014	0.0020
29	15.757	6Q-3M	-0.1036	-0.6973	0.0584	0.3970
30	16.389	4M-4Q	-0.2989	-0.0378	0.2749	0.0349
31	16.913	9Q-5M	0.0110	0.0084	-0.0079	-0.0062
32	17.545	2M-Q	7.1178	-4.9824	11.3260	7.9007
33	18.700	2Q	-18.0739	78.8608	12.3700	-53.5567
34	19.332	7M-8Q	-0.0015	-0.0001	0.0006	0.0003

i	hω <sub>i</sub> , MeV		Q	00	Q	20
			b <sub>i</sub>	a <sub>i</sub>	b <sub>i</sub>	$a_{l}$
35	19.855	5Q-2M	0.9875	1.7677	-0.6990	-1.2564
36	20.487	5M-5Q	-0.0634	0.0156	0.0196	-0.0047
37	21.010	8Q-4M	0.0044	0.0016	-0.0024	-0.0008
38	21.642	3M-2Q	0.6798	-0.9969	0.2118	-0.3093
39	22.165	11Q-6M	-0.0008	0.0004	-0.0001	0.0001
40	22.797	Q+M	0.8979	6.5434	1.6030	11.8635
41	23.952	4Q-M	-0.3578	-0.3010	2.4021	2.0305
42	24.584	6M-6Q	-0.0010	0.0007	-0.0020	0.0013
43	25.107	7Q-3M	-0.0283	0.0010	0.0851	-0.0028
44	25.739	4M-3Q	-0.0036	0.0150	0.0306	-0.1253
45	26.894	2M	-0.2367	-0.4352	0.7693	1.4230

Table 3. Fourier coefficients and energies for  $\dot{Q}_{00}(0)=5000, \dot{Q}_{20}(0)=18000$ 

i	hω, MeV		. Q	200	Q	20
		-	b <sub>i</sub>	$a_i$	b <sub>l</sub>	a <sub>i</sub>
0	0.000	1	0.000	248.004	0.000	-966.077
1	0.283	9M-13Q	-0.010	0.005	0.061	-0.033
2	0.952	3Q-2M	-8.682	-21.535	42.528	105.465
3	1.236	7M-10Q	0.001	0.000	0.084	-0.124
4	1.905	6Q-4M	-0.553	-0.574	0.865	0.897
5	2.189	5M-7Q	-0.062	0.229	0.310	-1.147
6	2.858	9Q-6M	0.116	0.052	-0.788	-0.357
7	3.141	3M-4Q	0.045	0.389	1.234	10.593
8	3.811	12Q-8M	0.010	0.001	-0.061	-0.015
9	4.094	M-Q	-12.323	-22.605	183.778	336.847
10	4.378	10M-14Q	-0.000	0.002	0.025	-0.020

i	hω, MeV		Q	00	Q	20
			b <sub>i</sub>	a <sub>i</sub>	bi	a <sub>i</sub>
11	4.764	15Q-10M	-0.001	0.002	0.014	-0.002
12	5.047	2Q-M	43.929	36.141	-87.113	-71.611
13	5.330	8M-11Q	-0.003	0.007	0.005	0.000
14	5.717	18Q-12M	-0.000	-0.001	0.001	0.003
15	6.000	5Q-3M	4.043	1.273	-14.550	-4.574
16	6.283	6M-8Q	-0.024	-0.100	0.162	0.671
17	6.953	8Q-5M	-0.201	0.015	1.112	-0.084
18	7.236	4M-5Q	-1.187	-1.679	3.013	4.258
19	7.906	11Q-7M	-0.032	0.012	0.132	-0.048
20	8.189	2M-2Q	33.679	21.708	-190.830	-122.828
21	8.472	11M-15Q	0.001	-0.001	-0.017	0.017
22	8.859	14Q-9M	-0.014	0.014	0.033	-0.058
23	9.142	Q	-170.626	-32.693	1783.589	340.434
24	9.425	9M-12Q	0.000	-0.007	0.021	0.031
25	10.095	4Q-2M	13.165	-2.585	102.969	-20.304
26	10.378	7M-9Q-	-0.033	-0.037	0.257	0.294
27	11.048	7Q-4M	1.595	-1.038	2.371	-1.547
28	11.331	5M-6Q	-0.579	-0.284	-1.120	-0.547
29	12.000	10Q-6M	-0.112	0.161	-0.197	0.284
30	12.284	3M-3Q	-7.164	-0.526	-24.352	-1.766
31	12.953	13Q-8M	-0.024	0.090	-0.015	0.033
32	13.237	М	361.277	-115.654	154.458	-49.621
33	13.520	10M-13Q	-0.032	-0.039	-0.002	-0.009
34	14.189	3Q-M	112.204	-93.180	-3.016	2.511
35	14.473	8M-10Q	-0.003	0.006	0.007	+0.002
36	15.142	6Q-3M	4.595	-8.523	-1.928	3.586

i	hω <sub>i</sub> , MeV		Q	200	Q	20
			, b <sub>i</sub>	$a_i$	b <sub>i</sub>	$a_i$
37	15.426	6M-7Q	0.216	-0.006	0.034	-0.002
38	16.095	9Q-5M	0.005	-0.057	-0.004	0.047
39	16.378	4M-4Q	-3.315	1.504	1.591	-0.724
40	17.331	2M-Q	23.410	-24.538	-21.116	22.195
41	18.001	15Q-9M	0.006	0.014	-0.006	-0.005
42	18.284	2Q	-46.772	117.573	30.189	-76.202
43	19.237	5Q-2M	0.056	12.158	-0.052	-8.678
44	19.520	7M-8Q	-0.054	0.031	0.024	-0.014
45	20.190	8Q-4M	0.237	0.580	-0.167	-0.407

The results of such calculations are demonstrated in Tables 1, 2, 3, where the eigenfrequencies  $\hbar\omega_i$  and the corresponding coefficients  $a_i$  and  $b_i$  of the functions  $Q_{20}$  and  $Q_{00}$  are shown for three variants of i.c. and  $\lambda = \lambda_{\rm Bohr}$ . Let us analyse in detail the first table. As one can see there are about 40 eigenfrequencies having the diapason of the amplitudes  $a_i$ ,  $b_i$  from  $10^{-3}$  to  $10^3$ , the dozen of them having this diapason from  $10^0$  to  $10^3$ . All these frequencies correspond to transitions between various levels  $E_{\rm v}$  of the nucleus, i.e., they can be represented as differences  $\hbar\omega_{\mu\nu} = E_{\mu} - E_{\nu}$ . So, it is necessary to perform some combinatorial analysis to find the eigenvalues  $E_{\rm v}$ . Of course the energies of GQR and GMR can be recognized immediately without any combinatorics. They are very close to that of calculated in the small amplitude approximation:  $E_2(\hbar\omega_{12})$  became 9.49 MeV instead of 9.78 MeV and  $E_0(\hbar\omega_{17})$  became 13.67 MeV instead of 13.84 MeV. So, we confirmed the well-known fact, that giant resonances are described very well in the small amplitude approximation.

It is very interesting to discover the multiphonon states. One can find two-three- and four-phonon states, corresponding to GQR. Their energies are  $\hbar\omega_{22}=2\cdot E_2=18.98$  MeV,  $\hbar\omega_{30}=3\cdot E_2=28.48$  MeV and  $\hbar\omega_{36}=4\cdot E_2=37.97$  MeV. There are two- and three-phonon states corresponding to GMR. Their energies are  $\hbar\omega_{29}=2\cdot E_0=27.34$  MeV and  $\hbar\omega_{37}=3\cdot E_0=41$  MeV. There is one two-phonon state consisting of the quadrupole and monopole phonons (its energy is  $\hbar\omega_{25}=E_2+E_0=23.16$  MeV). There are two three-phonon states consisting of: two quadrupole plus one monopole phonons  $\hbar\omega_{33}=2\cdot E_2+E_0=32.65$  MeV and two monopole plus one quadrupole phonons  $\hbar\omega_{35}=E_2+2\cdot E_0=36.83$  MeV.

It is not so difficult to show, that all the rest  $h\omega_i$  are just the differences of these (and more high lying) multiphonon states. The results of the combinatorial analysis are shown in the third columns of the tables.

The calculations with the  $\lambda = \frac{3}{4} \lambda_{\rm Bohr}$  show that the results are rather sensitive to the force constant. For example, the energies of GQR and GMR are increased by 1.2 MeV and 0.06 MeV, respectively, their strengths decreasing about 15%. The strengths of multiphonon states are decreased about 2 times and more. The comparison of the results of calculations with different i.c. shows that strengths of all the states are very sensitive to i.c., what is evident. Not so evident is the noticeable dependence of energies on i.c. We interpret it as the manifestation of the dynamical deformation of the nucleus. This deformation is rather large and depends on i.c. Analysing tables 1-3 one can notice the next rule: the more (the less) the initial values of  $Q_{00}$  or  $Q_{20}$  are chosen, the more (the less) the resulting amplitudes are obtained and the more of new frequencies appear.

The limit of maximum possible amplitudes is achieved at  $Q_{20}(0) \approx 20000$ . The calculations show that the maximum positive value of  $Q_{20}$  is ~1980 and the maximum negative value is ~2480. Which value of the deformation parameter  $\beta$  these amplitudes correspond to? To answer this question we derive the formula for the  $\beta$ -dependence of  $Q_{20}$  in the approximation of the sharp edge of a nucleus. By definition

$$Q_{20}(\beta) = n_0(\beta) \int_0^{2\pi} d\phi \int_0^{\pi} \sin \theta \, d\theta \int_0^{R(\theta,\phi)} (x_1^2 + x_2^2 - 2x_3^2) r^2 dr.$$
 (30)

Here  $R(\theta, \phi) = R_0(1 + \beta Y_{20}(\theta, \phi))$ ,  $x_1^2 + x_2^2 - 2x_3^2 = -4\sqrt{\frac{\pi}{5}} r^2 Y_{20}(\theta, \phi)$  and the density  $n_0(\beta)$  is defined as

$$n_0(\beta) = A \left\{ \int_0^{2\pi} d\phi \int_0^{\pi} \sin\theta d\theta \int_0^{R(\theta,\phi)} r^2 dr \right\}^{-1}.$$

Performing the simple but tedious calculations we get:

$$Q_{20}(\beta) = -4 \sqrt{\frac{\pi}{5}} n_0(\beta) R_0^5 \left\{ \beta + \frac{4}{7} \sqrt{\frac{5}{4\pi}} \beta^2 + \frac{15}{14\pi} \beta^3 + \frac{100}{77} \sqrt{\frac{5}{(4\pi)^3}} \beta^4 + \frac{25 \cdot 53}{77 \cdot 13(4\pi)^2} \beta^5 \right\},$$

$$n_0(\beta) = 3 \frac{A}{R_0^3} \left\{ 4\pi + 3\beta^2 + \frac{2}{7} \sqrt{\frac{5}{4\pi}} \beta^3 \right\}^{-1}.$$
(31)

With the help of these formulae we find, that the vibrations with the maximum amplitude correspond to the change of  $\beta$  from ~0.29 to ~-0.29. So, the shape of the nucleus changes during the vibrations from oblate to prolate. Further increasing of  $Q_{20}(0)$  leads to the instability: the amplitudes begin to grow infinitely. It is necessary to stress that due to the lack of the full self-consistency of our Hamiltonian this value of maximum  $\beta$  must be considered as the lower bound for  $\beta_{max}$ . By the way, the amplitudes presented on the figure correspond to  $\beta \cong 0.13$ .

The limit of small amplitudes is practically achieved for the sixth variant of i.c., where only GQR and GMR have the noticeable amplitudes and their energies are equal exactly to  $\sqrt{2}h\omega$  and  $2h\omega$ .

- 3.4. Hydrodynamical Limit. There is one more interesting solution of the system (20). It is the so-called «hydrodynamical limit». The Fermi liquid differs from the classic one by the existence of the Fermi surface deformation. So, if to suppose  $\Pi_{20}=0$ , the system (20) (without the last equation) will describe pure hydrodynamics. Its solution in the small amplitude approximation is very well known:  $E_2=0$ , i.e., there is no GQR in the classic hydrodynamics. However the exact solution gives the nonzero value:  $E_2=0.28$  MeV for  $Q_{20}(0)=3$ ,  $Q_{00}(0)=6100$ . This solution exists for initial conditions  $Q_{20}(0)<3.5$ ,  $Q_{00}(0)>6000$  and changes not very much in these limits. Including  $\Pi_{20}$  gradually one can observe the evolution of this solution. With this aim we multiplied  $\Pi_{20}$  in the third equation of the system (20) by a constant factor  $\alpha$ . When  $\alpha$  is changed gradually from 0 to 1,  $E_2$  grows gradually from 0.28 MeV at  $\alpha=0$  to the usual value of the GQR energy at  $\alpha=1$ .
- 3.5. Excitations Probabilities. The excitations probabilities can be calculated with the help of the classical formula for the intensity of the quadrupole radiation [9]:

$$Int = \frac{1}{180c^5} \sum_{i,j} \bar{D}_{i,j}^2, \qquad (32)$$

where  $D_{i,j} = eZ/A \left( 3J_{i,j} - \delta_{i,j} \sum_{s} J_{s,s} \right)$  Due to the axial symmetry of the Hamiltonian

$$D_{11} = D_{22}$$
,  $D_{33} = -2D_{11}$  and  $D_{i,j} = 0$  for  $i \neq j$ . Hence  $\sum_{i,j} D_{i,j}^2 = \frac{3}{2} D_{33}^2 = \frac{3}{2} \left(\frac{eZ}{A}\right)^2 Q_{20}^2$ .

Putting into (32) the Fourier expansion for  $Q_{20}$  and averaging over the greatest period of oscillations we get:

$$\overline{\operatorname{Int}} = \left(\frac{eZ}{A}\right)^2 \frac{1}{120c^5} \sum_{\alpha} \omega_{\alpha}^6 \frac{a_{\alpha}^2 + b_{\alpha}^2}{2} \equiv \sum_{\alpha} \overline{\operatorname{Int}}_{\alpha}.$$
 (33)

Dividing  $\overline{\operatorname{Int}}_{\alpha}$  by  $\hbar\omega_{\alpha}$  we obtain the radiation probability  $W_{\alpha}$ . Taking into account the relation between  $W_{\alpha}$  and the reduced probability [10] we find:

$$B_{\alpha}(E2) = \left(\frac{eZ}{A}\right)^2 \frac{5}{64\pi} \left(a_{\alpha}^2 + b_{\alpha}^2\right) = \left(\frac{Z}{A}\right)^2 \frac{125}{144} \frac{a_{\alpha}^2 + b_{\alpha}^2}{R^4} B_W, \tag{34}$$

where  $B_{\mathbf{w}}$  is Weisskopf unit.

Using here the values of  $a_{\alpha}$  and  $b_{\alpha}$  from Table 1 we can calculate the B(E2)-factors for GQR and multiphonon states:

$$B(E2, GQR) = 57.5B_{w}$$

$$B(E2, 2 \times GQR) \cong 6 \cdot 10^{-4} B(E2, GQR) = 0.03 B_W$$
.

The excitation probability of the two-phonon GQR is approximately three orders of magnitude less than that of the usual one-phonon GQR. The B(E2)-factor for the three-phonon state is six orders of magnitude less than that of the GQR.

# 4. One-Dimensional Model

To reach more deep understanding of rather unusual properties of our model (the dependence of eigenfrequences on initial conditions, the lack of an anharmonicity of a spectrum in spute of an anharmonic potential) we will consider here exactly soluble one-dimensional model of a harmonic oscillator with a monopole-monopole residual interaction. Its solution was found by Reinhardt and Schulz [11] in a rather complicated way. With the help of our method the solution becomes elementary.

The average field of the model (in the notations of [11]) is

$$V(x, t) = \frac{1}{2} m\omega_0^2 x^2 = \kappa(\langle x^2 \rangle - x_0^2)(x^2 - x_0^2/A), \qquad (35)$$

where in correspondence with our notations  $\omega_0 = \omega$ ,  $\langle x^2 \rangle = J_{11}(t)$ ,  $x_0^2 = J_{11}(0)$ . Following the rules described in section 2.1 one can derive the system of equations

$$m\ddot{J} + 2J[m\omega^2 + 2\kappa(J - J_0)] - \frac{2}{m}\Pi = 0,$$

$$\dot{\Pi} + mJ[m\omega^2 + 2\kappa(J - J_0)] = 0$$
(36)

with  $J = J_{11}(t)$ ,  $J_0 = J_{11}(0)$ ,  $\Pi = \Pi_{11}$ . The second equation of this system gives the integral of motion

$$\Pi + m^2 \omega^2 J + m \kappa J^2 - 2m \kappa J_0 J = \text{const.}$$
 (37)

The value of const can be fixed by the conditions of equilibrium. In the state of equilibrium  $J = J_0$ ,  $\Pi = \Pi_0$  and one has from (36) and (37):

$$2m\omega^{2}J_{0} - \frac{2}{m}\Pi_{0} = 0,$$
  

$$\Pi_{0} + m^{2}\omega^{2}J_{0} - m\kappa J_{0}^{2} = \text{const.}$$
(38)

Combining these two equations one finds:

$$const = 2m^2 \omega^2 J_0^2 - m \kappa J_0^2. (39)$$

Using (37), (39) and introducing new variable  $y = J - J_0$  one reduces the system (36) to the single equation

$$\ddot{y} + ay + by^2 = 0, (40)$$

with  $a = 4\left(\omega^2 + \frac{\kappa}{m}J_0\right)$ ,  $b = 6\frac{\kappa}{m}$ . This equation is integrated trivially to give

$$\left(\frac{dy}{dt}\right)^2 = -\frac{2}{3}by^3 - ay^2 - c_1,\tag{41}$$

where  $c_1$  is a constant of integration, which is determined by initial conditions. Having in mind, that y(0) = 0, one finds  $c_1 = -(y(0))^2$ . The solution of the equation (41) can be expressed in terms of the Jacobian elliptic function [12]:

$$y(t) = \eta_3 + (\eta_2 - \eta_3) \sin^2(\overline{\omega}t).$$
 (42)

Here  $\overline{\omega} = \frac{\omega}{x_o} \sqrt{\overline{\kappa}(\eta_1 - \eta_3)}$ ,  $\overline{\kappa} = \kappa \frac{x_0^2}{m\omega^2}$ ,  $\eta_i$  are the roots of the polynomial

$$P(y) = y^3 + \frac{3a}{2b}y^2 + \frac{3c_1}{2b}. (43)$$

The function  $sn(\phi)$  is a periodical one with a period  $\Delta \phi = 4K$ , K being the complete elliptic integral of a first kind:

$$\mathbf{K} = \int_0^{\pi/2} \frac{d\phi}{\sqrt{1 - k^2 \sin \phi}} \,, \tag{44}$$

where  $k^2 = \frac{\eta_2 - \eta_3}{\eta_1 - \eta_3}$ . Hence, the period of the function y(t) will be proportional to  $\Delta t = \frac{4K}{\omega}$  and the corresponding frequency will be proportional to  $\Omega = \frac{2\pi}{\Delta t} = \frac{\pi \overline{\omega}}{2K}$ . This

expression demonstrates very well the dependence of eigenfrequencies on initial conditions,

because it is evident that the roots of the polynomial (43) depend on  $c_1$ , which in its turn depends on  $\dot{y}(0)$ . The absence of any anharmonicity can be understood studying the trigonometrical expansion of the Jacobian function [13]:

$$\operatorname{sn}\overline{\omega}t = \frac{2\pi}{k\mathbf{K}} \sum_{n=1}^{\infty} \frac{q^{n-1/2}}{1 - q^{2n-1}} \sin(2n - 1) \frac{\overline{\omega}\pi}{2\mathbf{K}} t.$$

Here  $q = \exp(-\pi K'/K)$ , K' = K(k'),  $k' = \sqrt{1 - k^2}B$  This expansion contains only frequencies proportional to odd numbers of the basic frequency  $\Omega = \frac{\overline{\omega}\pi}{2K}$ . It is evident, that

sn<sup>2</sup> will contain frequencies  $n\Omega$  with even n only. So, the Fourier expansion of the function y(t) will contain only one basic frequency  $2\Omega$  and its satellites  $4\Omega$ ,  $6\Omega$  and so on. In the case of our two-dimensional problem of a coupled dynamics of monopole and quadrupole moments it is natural to expect the two basic frequencies  $\Omega_1$ ,  $\Omega_2$  and their satellites. Due to coupling there must be a lot of linear combinations of these frequencies:  $n_1\Omega_1 \pm n_2\Omega_2$ . As we have seen, such picture really takes place.

Let us compare our solution with that of Reinhardt and Schulz [11]. They have studied the collective 'variable r(t) which is connected with our variable y(t) by the relation  $y = x_0^2(r^2 - 1)$  (formula (3.28) of [11]). Their dynamical equation for r(t) reads (formulae (3.17), (3.29)):

$$\ddot{r} - \frac{\omega^2}{r^3} + \omega^2 [r + 2\overline{\kappa}(r^3 - r)] = 0. \tag{45}$$

Multiplying (45) by  $\dot{r}$  one easily transforms it into

$$\frac{d}{dt} \left\{ \frac{\dot{r}^2}{2} + \frac{\omega^2}{2r^2} + \omega^2 \left[ \frac{r^2}{2} + \overline{\kappa} \left( \frac{r^4}{2} - r^2 \right) \right] \right\} = 0, \tag{46}$$

demonstrating the existence of the integral of motion

$$\dot{r}^2 + \omega^2 \left[ \frac{1}{r^2} + r^2 + \overline{\kappa} (r^2 - 1)^2 \right] = c_2, \tag{47}$$

which expresses the energy conservation. This integral allows one to prove the equivalence of the equations (40) and (45). Really, putting  $y = x_0^2(r^2 - 1)$  and  $\ddot{y} = 2x_0^2(r\ddot{r} + \dot{r}^2)$  into (40) and eliminating the term proportional to  $\dot{r}^2$  with the help of the relation (47) one gets:

$$r\ddot{r} - \omega^2 \left[ \frac{1}{r^2} + r^2 + \overline{\kappa}(r^2 - 1)^2 \right] + c_2 + \frac{a}{2}(r^2 - 1) + \frac{b}{2}x_0^2(r^2 - 1)^2 = 0.$$
 (48)

This equation becomes equivalent to equation (45) if to take  $c_2 = 2\omega^2$ . With such value of  $c_2$  our integral of motion (47) will coincide with that of Reinhardt and Schulz only in the case when  $E_{\rm HF} = E_0$  (formula (3.30)). By the way, this requirement follows naturally from their condition of self-consistence (see the bottom of section 3.2 in their paper [11]).

### 5. Conclusion

Let us enumerate the main results of this paper. The set of nonlinear dynamical equations for quadrupole  $Q_{20}$  and monopole  $Q_{00}$  moments of nuclei is derived from the TDHF equation with the help of the method of Wigner function moments. Due to the simplicity of the used Hamiltonian all the derivations are performed exactly, without any approximations. These equations are solved numerically for  $^{208}\text{Pb}$ . It is found, that the functions  $Q_{20}(t)$  and  $Q_{00}(t)$  oscillate irregularly. Their Fourier analysis yields a lot of eigenfrequencies, which correspond to various differences of the energy levels. Combinatorial analysis allows one to find the giant quadrupole and monopole resonances and several multiphonon states constructed of these two resonances. It is shown that the reduced probability of the excitation of the two-phonon giant quadrupole resonance is three orders of magnitude less than that of the one-phonon GQR.

The theory can be modified to take into account spin degrees of freedom. In this case it will be possible to study a large amplitude motion with the rather realistic Nilsson potential. The extension to the description of excitations of higher multipolarities is straightforward.

### References

- Schuck P. Proc. of the Winter College on Fundamental Nucl. Phys., ICTP, Trieste, Italy, 1984, ed. K.Dietrich, M.Di Toro, H.J.Mang, vol.1, p.56.
- 2. Provoost D., Grummer F., Goeke K., Reinhard P.-G. Nucl. Phys., 1984, A431, p.139.
- 3. Klein A., Marshalek E.R. Rev. Mod. Phys., 1991, 63, p.375.
- 4. Wigner E. Phys. Rev., 1932, 40, p.749.
- 5. Balbutsev E.B. Sov. J. Part. Nucl., 1991, 22, p.159.
- 6. Balbutsev E.B., Molodtsova I.V. Sov. J. Nucl. Phys., 1989, 50, p.212.
- 7. Bohr A., Mottelson B. Nuclear Structure. Benjamin, New York, 1975, v.2.
- 8. Balbutsev E.B., Piperova J. Sov. J. Nucl. Phys., 1989, 50, p.961.
- 9. Landau L.D., Lifshits E.M. Theory of Field, Fizmatgiz, Moscow, 1962.
- 10. Ring P., Schuck P. The Nuclear Many Body Problem, Springer, Berlin, 1980.

- 11. Reinhardt H., Schulz H. Nucl. Phys., 1982, A391, p.36.
- 12. Smirnov V.I. Kurs visshey matematiki, Fizmatgiz, Moscow, 1958, v.3, part 2.
- 13. Gradshtein I.S., Ryzhik I.M. Tablitsy integralov, summ, ryadov i proizvedeniy, Fizmatgiz, Moscow, 1962.

УДК 539.12...142:539.125.4

# TEST OF THE ELLIS-JAFFE SUM RULE USING PARAMETRIZATION OF THE MEASURED LEPTON-PROTON ASYMMETRY

# A.P.Nagaitsev\*, V.G.Krivokhijine\*, I.A.Savin, G.I.Smirnov

It is shown that the values of the first moment of  $g_1^p(x)$  calculated from simultaneous fits of the SMC and E143 data on the asymmetries  $A_1^p(x)$  are below the Ellis-Jaffe prediction by more than  $7\sigma$ .

The investigation has been performed at the Laboratory of Particle Physics, JINR.

# Проверка правила сумм Эллиса-Джаффе с использованием параметризации данных по лептон-протонной асимметрии

# А.П.Нагайцев и др.

Показано, что величины первого момента от  $g_1^p(x)$ , вычисленные из одновременной аппроксимации SMC и Е 143 данных по асимметрин  $A_1^p(x)$ , находятся ниже предсказаний правила сумм Эллиса-Джаффе более чем на  $7\sigma$ .

Работа выполнена в Лаборатории сверхвысоких энергий ОИЯИ.

### 1.Introduction

It has been found from the measurements of the spin-dependent structure function  $g_1^p(x)$  of the proton by the SMC [1] and E143 [2] that the value  $\Gamma_1^p$ , which is the first moment of  $g_1^p(x)$ , is below the Ellis-Jaffe sum rule prediction. We quote in detail the results of Refs. [1], [2], because they are important for our discussion.

1.1. SMC. The result for the first moment of  $g_1^p(x)$  at  $\langle Q^2 \rangle = 10 \text{ GeV}^2$  is

$$\Gamma_1^p = \int_0^1 g_1^p(x)dx = 0.136 \pm 0.011 \text{ (stat.)} \pm 0.011 \text{ (syst.)}.$$
 (1)

<sup>\*</sup>Granted by Russian Fund of Federal Research

The integral over the measured x range is

$$\int_{0.003}^{0.7} g_1^p(x)dx = 0.131 \pm 0.011 \pm 0.011.$$
 (2)

The values of integrals over unmeasured x regions are

$$\int_{0}^{0.003} g_1^{p}(x)dx = 0.004 \pm 0.002, \quad \int_{0.7}^{1} g_1^{p}(x)dx = 0.001 \pm 0.001.$$
 (3)

The corresponding Ellis-Jaffe prediction corrected for QCD effects [3] is:

$$\Gamma_1^p = 0.176 \pm 0.006.$$
 (4)

SMC has evaluated  $g_1^p(x)$  from virtual photon-proton asymmetry  $A_1^p(x, Q^2)$  averaged over  $Q^2$  in each bin using the relation:

$$g_1^p(x) \cong \frac{A_1^p(x, Q^2) F_2^p(x, Q^2)}{2x (1 + R(x, Q^2))} \cong A_1^p(x) F_1^p(x, Q^2). \tag{5}$$

 $A_1^p(x,Q^2)$  is assumed to be independent of  $Q^2$ . The unpolarized structure functions  $F_2^p(x,Q^2)$  and  $R(x,Q^2)$  were taken from parametrizations [4] and [5], respectively, for the average  $\langle Q^2 \rangle = 10$  GeV<sup>2</sup> in the SMC kinematic region. The virtual photon-proton asymmetry  $A_1^p$  is related to the measured muon-proton asymmetry  $A_1^p$ :

$$A^{p} = \frac{\sigma^{\uparrow\downarrow} - \sigma^{\uparrow\uparrow}}{\sigma^{\uparrow\downarrow} + \sigma^{\uparrow\uparrow}},\tag{6}$$

$$A_1^p = \frac{A^2}{D} - \eta A_2^p, \tag{7}$$

where  $\sigma^{\uparrow\downarrow}(\sigma^{\uparrow\uparrow})$  is the cross section for the longitudinally polarized muons scattering on protons polarized opposite (along) to the muon momentum, D and  $\eta$  are the kinematic factors. SMC has shown in the separate experiment [6] that asymmetry  $A_2^P$  arising from the interference between virtual photons with transverse and longitudinal polarizations is compatible with zero within statistical errors. In addition, since coefficient  $\eta$  in the SMC kinematic region is small, product  $\eta A_2^P$  can be neglected in Eq. (7). So, with this assumption asymmetry  $A_1^P$  is directly proportional to the measured  $A_2^P$ :

$$A_1^p \cong \frac{A^p}{D} \,. \tag{8}$$

1.2. E143. The result for the first moment of  $g_1^p(x)$  at  $\langle Q^2 \rangle = 3$  is

$$\Gamma_1^p = 0.127 \pm 0.004 \text{(stat.)} \pm 0.010 \text{(syst.)}.$$
 (9)

The integral over the measured range is

$$\int_{0.029}^{0.8} g_1^p(x) dx = 0.120 \pm 0.004 \pm 0.008.$$
 (10)

The values of integrals over unmeasured x regions are

$$\int_{0}^{0.029} g_1^p(x) dx = 0.006 \pm 0.006, \quad \int_{0.8}^{1} g_1^p(x) dx = 0.001 \pm 0.001.$$
 (11)

The corresponding Ellis-Jaffe prediction corrected for QCD effects [3] is:

$$\Gamma_1^p = 0.160 \pm 0.006.$$
 (12)

E143 has evaluated  $g_1^p$  from the measurements of  $A_{\parallel}$  and  $A_{\perp}$  asymmetries for the scattering of the longitudinally polarized electrons on the target polarized parallel and transverse to the beam direction:

$$\frac{g_1^p}{F_i^p} = D^{-1}(A_{\parallel} + \tan(\Theta/2)A_{\perp}), \tag{13}$$

where  $\Theta$  is the electron scattering angle. This ratio is related to the virtual photon-proton asymmetry  $A_1^p$ :

$$A_1^p = \frac{g_1^p}{F_1^p} - \gamma^2 \frac{g_2^p}{F_1^p}, \quad \gamma^2 = \frac{Q^2}{\sqrt{2}} << 1$$
 (14)

and with the same level of confidence as for SMC, we can neglect product  $\gamma^2 g_2^p / F_1^p$  and obtain the same approximate relation as Eq.(5):

$$A_1^p \cong \frac{g_1^p}{F_1^p} \,. \tag{15}$$

Calculating  $\Gamma_1^p$  from  $g_1^p/F_1^p$ , in E143 it was assumed that the last ratio is independent of  $Q^2$ . Such an assumption was justified by observing good agreement between SLAC and SMC data taken at different  $Q^2$ .

The two experiments obtained  $\Gamma_1^P$ , which is below the Ellis-Jaffe sum rule prediction by more than two standard deviations. These discrepancies could be caused by some physics effects not taken into account by the Ellis-Jaffe model or due to imperfection of the data and their analysis. Since in terms of standard deviations the difference between the data and theory is not significant, it is worth-while to examine possible experimental problems. One of them is a «nonsmoothness» in x behaviour of  $A_1^P$  present in both experiments and which is difficult to explain by statistical errors. It might be produced by possible incorrectable point-to-point systematic fluctuations. On the other hand, both experiments did not take into account the theoretical prediction  $A_1^P(x=1)=1$  while extrapolating the data to the unmeasured region  $0.7 < x \le 1$ . These two observations motivated our study of the changes in the  $\Gamma_1^P$  when the latter is calculated with the constraint  $A_1^P(1)=1$  and with smooth input  $A_1^P(x)$ . Such an approach has been used in paper [10] for discussions of the Bjorken sum rule tests.

# 2. Calculation of $\Gamma_1^p$

We calculate the first moment of  $g_1^p$  as follows:

- 1) The x-dependence of  $A_1^p$  is parametrized by function  $A^f(x)$  (the form of the function will be discussed later) with some free parameters. As long as values  $A_1^p(x, Q^2)$  and  $g_1^p/F_1^p$  measured in SMC and E143 are independent of  $Q^2$ , we can fit the data from two experiments simultaneously.
  - 2) This function  $A^f$  is used for calculations of  $g_1(x)$  and its integral:

$$g_1^p(x) \cong A^f(x, P_1, P_2) \frac{F_2^p(x, Q^2)}{2x(1 + R(x, Q^2))} \cong A^f(x, P_1, P_2) F_1^p(x, Q^2),$$
 (16)

where we have used for  $F_2^p(x, Q^2)$  the NMC parametrization [4] and the SLAC parametrization [5] for  $R(x, Q^2)$  at given  $Q^2$ . Then

$$\Gamma_1^P = \int_0^1 g_1^P dx = \int_0^1 A^f(x, P_1, P_2, ...) F_1^P(x) dx,$$
(17)

where  $P_1, P_2, \ldots$  are parameters obtained from fit of the measured  $A_1^P(x)$ . The error of the integral from Eq.(17) is calculated using errors of the parameters taken from the fits (see Section 4).

# 3. Parametrization of A

3.1. The Choice of Functions for Fitting. We have suggested that the form of the parametrization functions should be the simplest one with the minimal number of parameters. These functions must meet two requirements:  $A_1^p(0) = 0$  and  $A_1^p(1) = 1$  taken from theoretical predictions [7, 8]. Two functions have been chosen out of many:

$$A_1^f(x) = \frac{P_2}{2} \cdot (x + x^{P_1}),\tag{18}$$

$$A_2^f(x) = P_2 \cdot x^{P_1}, \tag{19}$$

where  $P_1$ ,  $P_2$  are free parameters.

3.2. The Test of Agreement between SMC and E143 Data. To test the consistency of the SMC data on  $A_1^p$  and the E143 data on  $g_1^p/F_1^p$ , we have performed fits with functions from

Table 1. Separate fits of the SMC and E143 data using functions from Eqs.(18), (19)

The form of function	Experiment	$P_1$	$\Delta P_1$	P <sub>2</sub>	$\Delta P_2$	$\chi^2/d.o.f$
$A_1^f(x)$	SMC	0.551	0.084	0.988	0.158	0.58
	E143	0.625	0.038	1.100	0.054	1.43
$A_2^f(x)$	SMC	0.665	0.082	0.888	0.172	0.58
	E143	0.747	0.032	1.043	0.060	1.38

Table 2. Test of the systematic shift between the SMC and E143 data

The value of P <sub>2</sub>	Function	$\chi^2/d.o.f.$	$P_1$	$\Delta P_1$	P <sub>2</sub>	$\Delta P_2$
a) P <sub>2</sub> is free for E143	$A_1^f(x)$	1.167	0.599	0.031	1.068	0.046
$P_2 = 1$ for SMC	$A_2^f(x)$	1.123	0.732	0.025	1.016	0.043
b) P <sub>2</sub> is free fro SMC and	$A_1^f(x)$	1.227	0.560	0.016	1.004	0.087
$P_2 = 1$ for E143	$A_2^f(x)$	1.126	0.725	0.012	1.005	0.087

Eqs.(18), (19) for each experiment separately taking into account only statistical errors. From the results of the fits which are shown in Table 1 we conclude that the data are consistent because the values of parameters  $P_1$  and  $P_2$  are the same within the errors.

Table 1 also shows that within the errors  $P_2 \approx 1$  to be expected if the theoretical prediction  $A_1^P(1) = 1$  is valid. So, we can use  $P_2 = 1$  unless there is a systematic shift between the SMC and E143 data. It was checked by fitting the data simultaneously for two cases according to different assumptions on  $P_2$ :

- 1)  $P_2 = 1$  for the SMC data and free for the E143 data;
- 2)  $P_2$  is free for the SMC data and  $P_2 = 1$  for the E143 data.

Table 2 shows that within the errors  $P_2 \approx 1$  as expected if there is no systematic shift between the data, which justifies the use  $P_2 = 1$  for further fits.

3.3. The Results of Fitting. The experimental points for fits were taken either with statistical errors only or with statistical and systematic errors combined.

Table 3 and Figures 1, 2 show the results of the fits of the SMC and E143 data taken either separately or simultaneously (SMC+E143) by Eqs. (18), (19) assuming that  $P_2 = 1$ .

Table 3. Separate and simultaneous fits of the data on  $A_1$  taken with:

a) the statistical errors only;
b) statistical and systematic errors combined linearly;
c) statistical and systematic errors combined in quadratures

The form		SMC			E143			SMC+E14	3
of function	P <sub>1</sub>	$\Delta P_1$	$\chi^2/d.o.f.$	$P_1$	$\Delta P_1$	$\chi^2/d.o.f.$	$P_1$	$\Delta P_1$	$\chi^2/d.o.f$
a) $A_1^f(x)$	0.556	0.044	0.524	0.561	0.016	1.509	0.560	0.015	1.192
b) $A_1^f(x)$	0.562	0.067	0.252	0.569	0.025	0.673	0.568	0.024	0.537
c) $A_1^f(x)$	0.559	0.050	0.431	0.569	0.016	1.197	0.565	0.018	0.950
a) $A_2^f(x)$	0.712	0.036	0.560	0.726	0.012	1.344	0.725	0.011	1.092
b) $A_2^f(x)$	0,717	0.054	0.270	0.730	0.019	0.596	0.728	0.018	0.537
c) $A_2^f(x)$	0.715	0.041	0.460	0.728	0.014	1.059	0.727	0.013	0.866

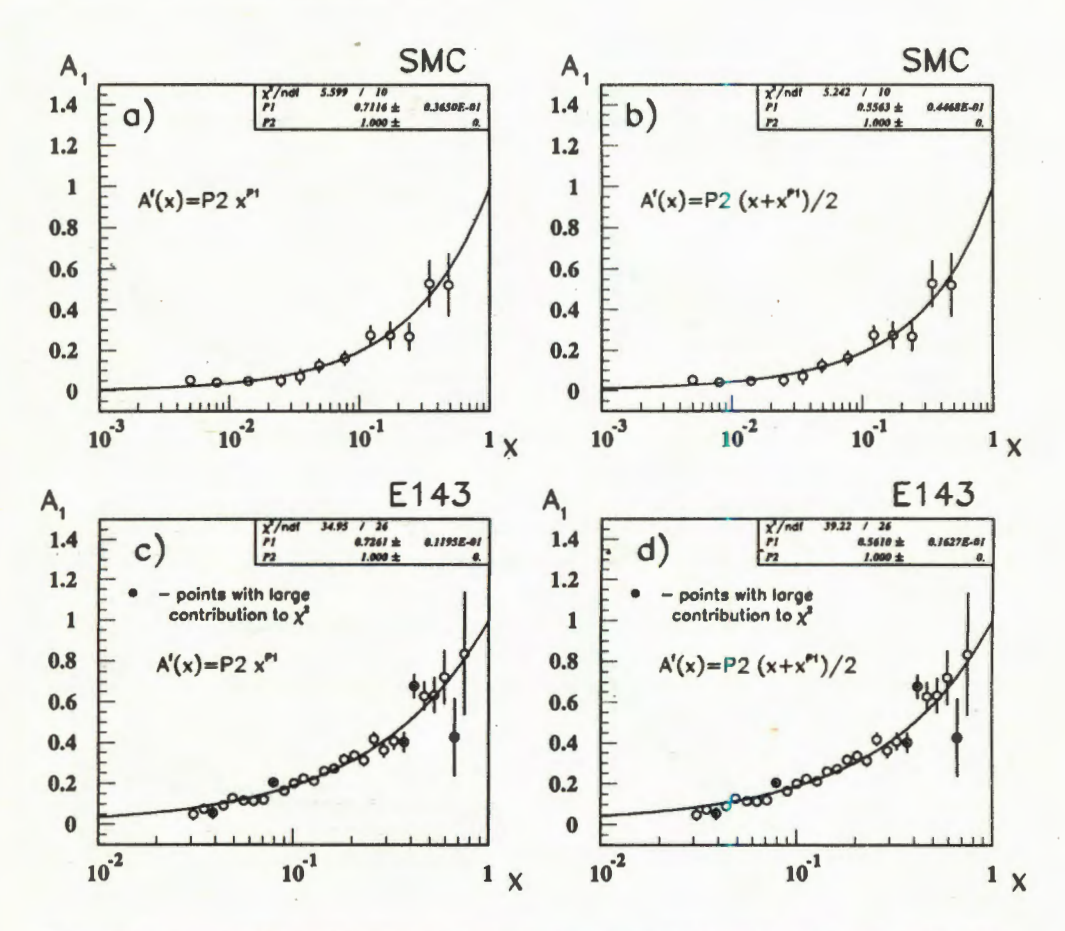


Fig.1. The approximations of lepton-proton asymmetry measured by the SMC and E143. The statistical errors are taken only

One can see that both fits yield consistent results for the free parameter  $P_1$  when the same function is used. From  $\chi^2$  values we can conclude that the data from both experiments are very well parametrized using the simplest functions with one free parameter. We cannot make the choice between the two functions because values  $\chi^2/d.o.f.$  are rather good in both cases. They are however worce for the E143 data indicating the presence of some systematic point-to-point fluctuations. For example, the points at x = 0.039, 0.079, 0.370, 0.416 and 0.666 (marked as dark points in Figs. 1c and 1d) give respectively 3.2, 5.9, 3.6, 5.6 and 3.2 units to  $\chi^2$  of the total 34.95 for 26 degrees of freedom. These contributions are largely reduced if the systematic errors (compare  $\chi^2/d.o.f.$  in Table 3) are taken into account.

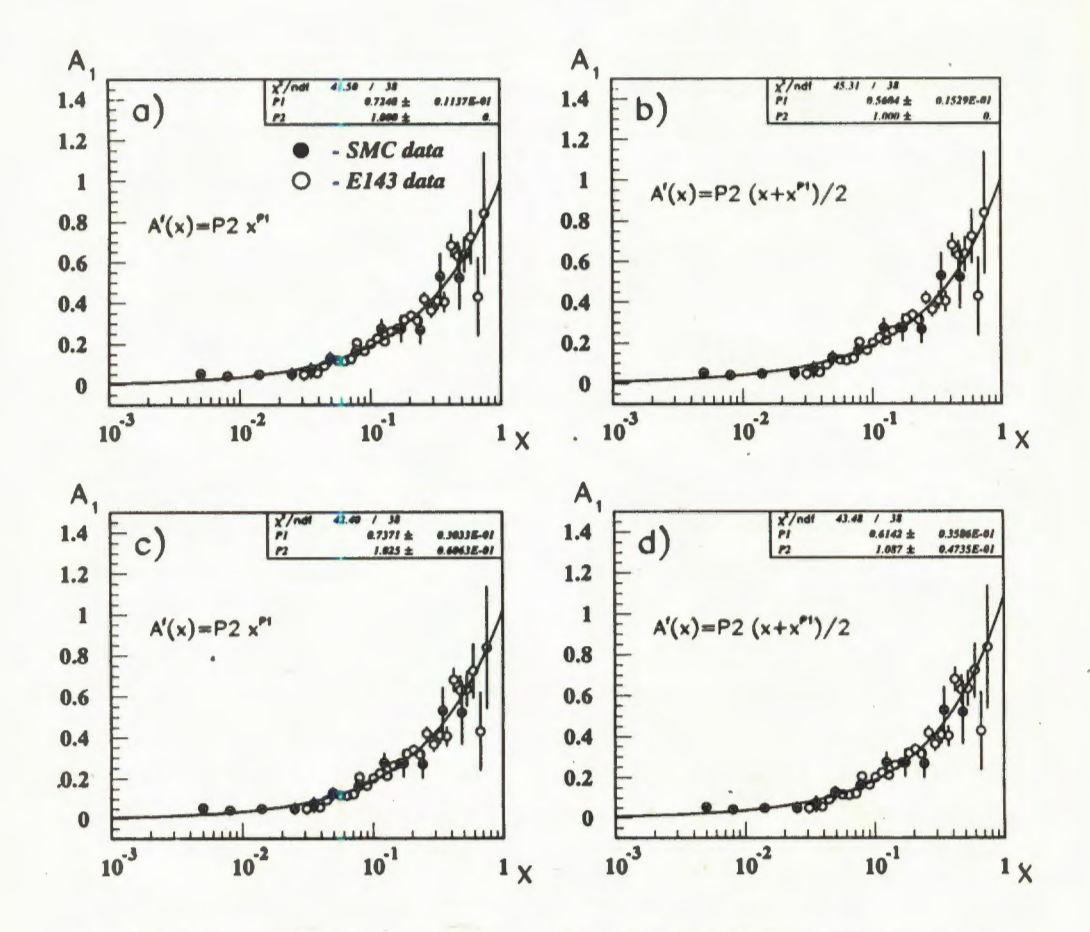


Fig.2. The approximations of proton asymmetry for the (SMC+E143) data. The statistical errors are taken only. The fits c) and d) were performed using functions with two free parameters

# 4. The First Moment of $g_1^p$

The functions with parameters of Table 3 were used to calculate integrals from Eq.(17). For the SMC and E143 data the structure functions  $F_2$  and R have been taken at  $Q^2 = 10$  and  $3 \text{ GeV}^2$ , respectively. The integral  $\Gamma_1^P$  for (SMC+E143) data has been calculated using the parameters of the simultaneous fit (column (SMC+E143), Table 3) and structure functions  $F_2$  and R at  $Q^2 = 5 \text{ GeV}^2$ . Uncertainties of the integrals were calculated

Table 4. The values of integrals  $\Gamma_1^p$  for the SMC data on  $A_1$  ( $\langle Q^2 \rangle = 10$  GeV <sup>2</sup>) taken with: a) statistical errors only; b)statistical and systematic errors combined in quadratures

The form of A <sup>f</sup> function	Γ,	$\int\limits_{0.003}^{0.7} g_1^p(x) dx$	$\int\limits_{0}^{0.003} g_1^p(x) \ dx$	$\int\limits_{0.7}^{1}g_{1}^{p}(x)\;dx$
a) $A_1^f(x)$	0.142±0.013	0.130±0.010	0.010±0.003	0.0010±0.0004
b) $A_1^f(x)$	0.141±0.015	0.129±0.011	0.010±0.004	0.0020±0.0004
a) $A_2^f(x)$	0.139±0.012	0.131±0.010	0.006±0.002	0.0020±0.0004
b) $A_2^f(x)$	0.138±0.013	0.130±0.011	0.006±0.002	0.0020±0.0004

Table 5. The values of integrals  $\Gamma_1^p$  for the E143 data on  $A_1$  ( $\langle Q^2 \rangle = 3$  GeV  $^2$ ) taken with:

a) statistical errors only;
b)statistical and systematic errors combined in quadratures

The form of A <sup>f</sup> function	$\Gamma_1^p$	$\int_{0.029}^{0.8} g_1^p(x)  dx$	$\int\limits_{0}^{0.029}g_{1}^{p}(x)\ dx$	$\int\limits_{0.8}^{1}g_{1}^{p}(x)dx$
a) $A_1^f(x)$	0.129±0.04	0.106±0.002	0.022±0.002	0.0010±0.0004
b) $A_1^f(x)$	0.127±0.004	0.105±0.002	0.021±0.002	0.0010±0.0004
a) $A_2^f(x)$	0.125±0.003	0.107±0.002	0.016±0.001	0.0020±0.0004
b) $A_2^f(x)$	0.124±0.003	0.107±0.002	0.016±0.001	0.0010±0.0004

Table 6. The values of integrals  $\Gamma_1^p$  for the SMC+E143 data on  $A_1$  ( $Q^2 = 5$  GeV  $^2$ ) taken with: a) statistical errors only; b)statistical and systematic errors combined in quadratures

The form of Affunction	$\Gamma_1^p$	$\int\limits_{0.003}^{0.8} g_1^p(x) \ dx$	$\int\limits_{0}^{0.003} g_{1}^{p}(x)  dx$	$\int\limits_{0.8}^{1}g_{1}^{p}(x)\ dx$
a) $A_1^f(x)$	0.133±0.004	0.124±0.003	0.008±0.001	0.0010±0.0004
b) $A_1^f(x)$	0.132±0.004	0.124±0.003	0.007±0.001	0.0010±0.0003
a) $A_2^f(x)$	0.128±0.003	0.123±0.003	0.040±0.003	0.0010±0.0003
b) $A_2^f(x)$	0.128±0.004	0.123±0.003	0.004±0.001	0.0010±0.0003

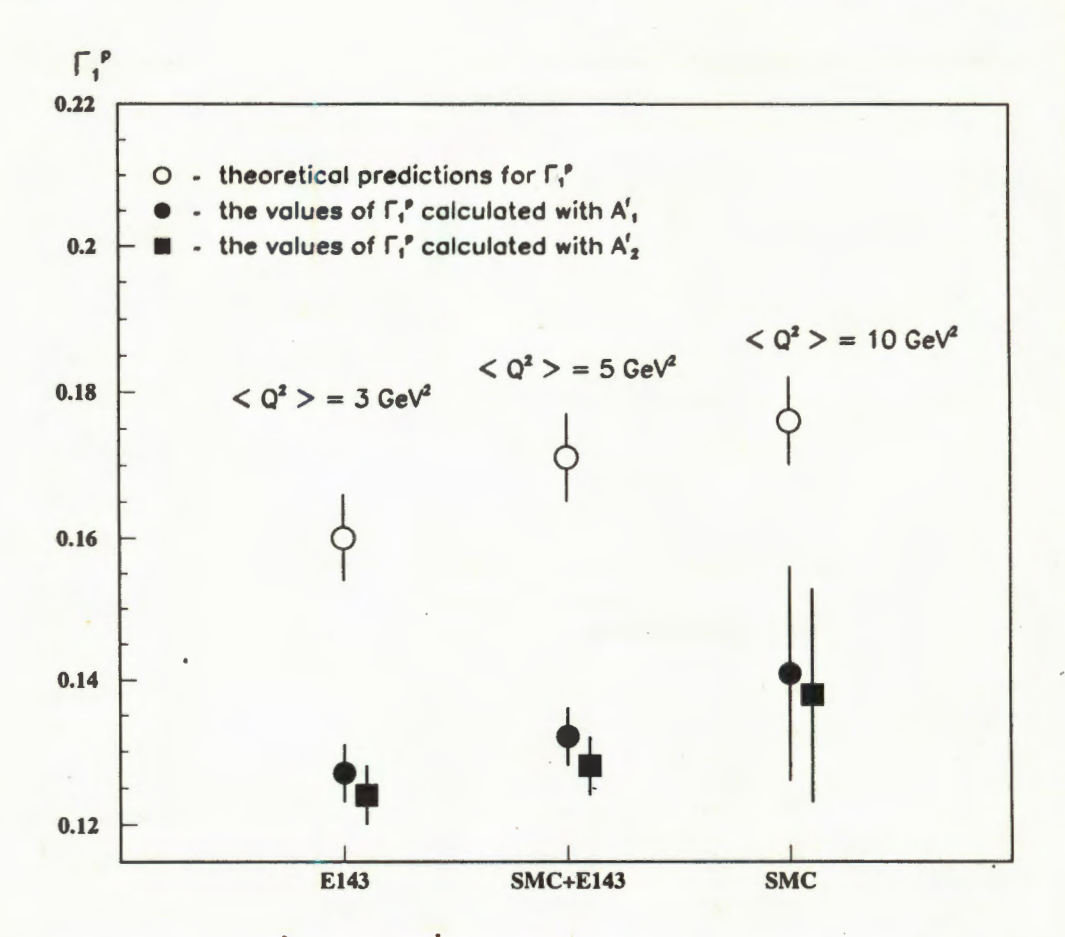


Fig.3. The comparison between theoretical predictions for  $\Gamma_{\rm I}^P$  and values obtained with the proposed method and errors  $\Delta\Gamma_{\rm I}^P$  estimated from statistical and systematic errors of the data combined in quadratures

by shifting average value of the parameter  $P_1$  by +/- one standard deviation:  $(P_1 - \Delta P_1)$  and  $(P_1 + \Delta P_1)$ . The results of calculations are presented in Tables 4—6. As it is seen from Tables 4 and 5, the integrals over the entire region calculated by us coincide within the errors with those from publications [1, 2].

We have also calculated the integrals for the measured and unmeasured x range to compare our results with those from Refs. [1, 2] (see Eqs.(2), (3) and Eqs. (10), (11)). The integrals over the measured x range for the SMC data calculated by us and in Ref. [1] are

the same, but extrapolation to x=0 is understimated in Ref. [1]. For the E143 data the integrals over the measured region are overstimated in Ref. [2] while the extrapolation to x=0 is largely underestimated. The results for the E143 measured region have smaller errors than those in paper [2] due to obvious reasons related to substitution of the experimental points by a smooth parametrization and additional constraints at x=0 and x=1. We have also computed  $\Gamma_1$  from the SMC and E143 data at a common value of  $Q_2=5$  GeV<sub>2</sub> by fitting simultaneously reevaluated values of  $g_1(x)$ . Reevaluation of  $g_1(x)$  has been done in the same way as in [9]. The results are to be compared with the Ellis-Jaffe prediction for  $\Gamma_1$  at 5 GeV<sub>2</sub>, which is  $0.171\pm0.006$  (see Figure 3). The comparison between theoretical predictions on  $\Gamma_1^p$  and the values obtained with the proposed method are also presented in Figure 3.

### 5. Discussion

- 1. It is shown that lepton-proton asymmetry from the SMC and E143 data fitted either separately or simultaneously can be parametrized using the simplest functions with one free parameter only. The SMC and E143 data are in agreement with the theoretical predictions  $A_1^p(x=0) = 0$ ,  $A_1^p(x=1) = 1$ . These constrains can be used in data parametrization.
- 2. The method to calculate  $\Gamma_1^P$  from Eq.(10) using parametrization of asymmetry  $A_1^P(x)$  is a natural generalization of the  $g_1^P(x)$  calculations from Eq.(5), when parametrizations  $F_2^P(x, Q^2)$  and  $R(x, Q^2)$  are used instead of experimental values. The values of  $\int g_1^P(x) dx$  calculated with this method for the entire x range are in agreement with the published ones:

	$\Gamma_1^p$	$\Gamma_{i}^{p}$	
	published value	this paper	
SMS data	$0.136 \pm 0.016$	$0.141 \pm 0.015$	
E143 data	$0.127 \pm 0.011$	$0.127 \pm 0.004$	

where the statistical and systematic errors are combined in quadratures.

3. The use of the parametrization of the measured asymmetries with physics constraints at x = 0 and x = 1 can be helpful in revealing unaccounted systematic errors in the data. For

example, the comparison of  $\int g_1^p(x) dx$  over the measured x range with that of Ref. [2] (E143) indicates that the last one is largely overestimated:

E143[2] This paper
$$\int_{0.029}^{0.8} g_1^p(x) dx \qquad 0.120 \pm 0.009 \qquad 0.105 \pm 0.003 .$$

We explain larger value of the integral from Ref. [2] by pretty large fluctuations of some data pionts at intermediate x. Due to the same reason the unconstrained fit (free  $P_2$ ) of the E143 data yields  $A_1^p(x=1) > 1$  (see Figs. 2c, 2d).

4. The parametrization of the asymmetries with the constraints at the boundaries provides a law for the extrapolations to the unmeasured low x and high x regions. This law is suggested by the data themselves, which we consider as more justified than making assumptions similar to those of Refs. [1, 2]. We find, for example, that E143 underestimates the low x contribution to the integral:

E143 paper This paper
$$\int_{0.0}^{0.029} g_1^p(x) dx \qquad 0.006 \pm 0.004 \qquad 0.021 \pm 0.003$$

This difference can serve as an argument to perform better measurements in the low x range for the proper choice of the parametrization.

5. The  $\Gamma_1^p$  calculated from the parametrized asymmetries with the constraints at the boundaries have smaller errors than those of Refs. [2, 9]. This indicates overestimation of possible systematic errors in these papers which devaluates the results of the measurements when compared to the Ellis-Jaffe predictions.

The proposed method allows one to demonstrate, that the conclusion of Ref. [2] that  $\Gamma_1^p$  is more than two standard deviations velow the Ellis-Jaffe sum rule predictions is dominated by systematic errors. The values of the first moment of  $g_1^p$  calculated by the proposed method from SMC and E143 data are also smaller than theoretical predictions, but the significance of deviation from them is now larger. For example, the integrals  $\Gamma_1^p$  calculated from the fits of the SMC, E143 and (SMC+E143) data on  $A_1^p$  (taken with statistical and systematic errors combuned in quadratures) are below the Ellis-Jaffe predictions by 2.5, 10 and 9 $\sigma$ , respectively. These results can be considered as a clear proof of the violation of the Ellis-Jaffe sum rule.

- 6. The value of  $\Gamma_1^P$  depends only slightly on the  $A_{1,2}^f$  parametrization and the present accuracy of the data does not permit one to choose between them.
- 7. Concerning the shortcomings of the method it should be emphasized that the calculation of the errors for  $\Gamma_1^p$  can be improved using a more sophisticated procedure for the treatment of experimental errors and their correlations. But we believe that this procedure will not change substantially the above conclusions. Our belief is based on the comparison of the  $P_1$  and  $\Delta P_1$  values given in Table 3. For the Table 3 (line b) results we have taken each experimental point with the error equal to the linear sum of the statistical and systematic errors, i.e., the upper limit of the possible error; using  $P_1$  and  $\Delta P_1$  from these fits for the estimations of the  $\Gamma_1^p$  and  $\Delta \Gamma_1^p$  we have found that difference between the SMC+E143 data and the Ellis-Jaffe prediction will be 7.5 $\sigma$  instead of 9 $\sigma$  obtained in case of more common treatment of errors.

### Acknowledgments

The authors are grateful to the members of the Spin Muon Collaboration for valuable discussions and recommendations. One of us (IS) is grateful to Profs. J.P.Burq and G.Smadja for the support at the Institute de Phisique Nucleaire de Lyon where this work has been initiated.

This work was supported in part by a grant of the Russian Foundation for Fundamental Research (A.P.Nagaitsev, V.G.Krivokhijine).

### References

- 1. SMC, Adams D. et al. Phys. Lett., 1994, B329, p.399.
- E143, Abe K. et al. Phys. Rev. Lett., 1995, 74, p.346, E143, Abe K. et al. Report No. SLAC-PUB-6508, 1994.
- Kodaira J. et al. Phys. Rev., 1979, D20, p.627; Kodaira J. et al. Nucl. Phys., 1979, B159, p.99; Kodaira J. Nucl. Phys., 1980, B165, p.129; Larin S.A. et al. Phys. Rev. Lett., 1991, 66, p.862.
- 4. NMC. Amaudruz P. et al. Phys. Lett., 1993, B316, p.429.

- 5. Whitlow L.W. et al. Phys. Lett., 1990, B250, p.193.
- 6. SMC, Adams D. et al. Phys. Lett., 1994, B336, p.125.
- 7. Brodsky S.J. et al. SLAC PUB 6087, 1994
- 8. Ellis J., Karliner M. Phys. Lett., 1988, B213, p.73.
- 9. SMC, Bonner B.E. et al. Phys. Lett., 1994, B320, p.400.
- 10. Indumathi D. Z. Phys., 1994, C64, p.439.